Localised crustal deformation along the central North Anatolian Fault Zone revealed by joint inversion of P-receiver functions and P-wave polarisations

Christian Schiffer[1,2]*, Tuna Eken[3], Stéphane Rondenay[4], Tuncay Taymaz[3],

1 Department of Earth Sciences, Durham University, Science Site, DH1 3LE, Durham, UK

2 Department of Earth Sciences, Uppsala University, 752 36 Uppsala, Sweden

3 Department of Geophysical Engineering, The Faculty of Mines, Istanbul Technical University, Maslak 34469, Istanbul, Turkey

4 Department of Earth Science, University of Bergen, Allegaten 41, N-5007 Bergen, Norway

Abstract

The North Anatolian Fault Zone (NAFZ) is a major plate boundary that separates the Eurasian plate to the north from the Anatolian plate to the south and is associated with powerful damaging earthquakes. Despite numerous studies of the crust and upper mantle across the NAFZ, our understanding of the exact mechanisms and distribution of deformation with depth is still limited. Accurate models of the crustal velocity structure are key to assess seismic hazard associated with strike-slip deformation. Here, we address this need by employing a novel method that jointly inverts receiver function waveforms and P-wave polarisations to recover S-wave velocity structure from the surface to the upper mantle. The method is applied to a dense teleseismic dataset collected across a segment of the central NAFZ in Turkey. The results provide important new constraints on the sedimentary thickness, depth to basement and Moho discontinuity beneath the region. Our estimates of uppermost sedimentary thickness range from 0 km in some areas (e.g. beneath the Central Pontides) to 6 km in the Çankırı Basin. Smaller basins are scattered along the NAFZ. A similar pattern is observed for the basement depth, with values exceeding 10 km beneath the Çankırı Basin, where the Moho is shallowest with a depth of ~32 km. The Moho reaches a maximum depth of ~42 km beneath the Central Pontides. Most other areas have an average Moho depth of 35-38 km. The results reveal clear structural-tectonic relationships in the crust: areas of fundamentally different sedimentary and crustal architecture are bounded by faults and suture zones. The NAFZ appears to accommodate small-

31 scale basin and basement-highs, and acts as a thick-skinned (i.e., full crustal-scale) boundary
32 between laterally displaced crustal blocks to the north and south. Seismicity clusters are centred
33 on areas of low Vp/Vs ratios that may be representative of weak zones.

34

35 Keywords: **Composition and structure of the continental crust, Joint inversion, Body waves, Crustal**
36 **imaging**

37

1. Introduction

39 Active continental fault zones have been the focus of extensive scientific attention owing to
40 their seismic hazard potential. Continental strike-slip faults can reach lengths of hundreds of
41 kilometres and may accommodate large deformation (Molnar and Dayem, 2010). The deep
42 structure of strike-slip fault zones and distribution of deformation is still a matter of debate. It
43 is unclear whether shear zones remain narrow and localised in the lower crust and upper mantle
44 or whether they expand into wide, distributed deformation bands at depths (Platt and Behr,
45 2011), possibly accommodated by lower crustal ductile flow (Bürgmann and Dresen, 2008). A
46 key diagnostic is the presence or absence of a large and abrupt Moho response beneath a fault
47 zone, which could hint at whether deformation is accommodated at depth via brittle or ductile
48 behaviour, respectively (Weber et al., 2004; Wilson et al., 2004; Zhu, 2000). Which process
49 dominates, in turn, has important consequences on the distribution of seismicity along
50 continental fault zones.

51 The North Anatolian Fault Zone (NAFZ) is a prominent example of an active continental
52 strike-slip fault and forms an important part of the complex tectonic setting in the eastern
53 Mediterranean and Anatolia. The recent tectonic evolution of this region is dominated by the
54 Cenozoic closure of the Tethys Ocean and subsequent convergence of the Arabian and Eurasian
55 Plates. At the same time, the African Plate converges and subducts northward beneath Anatolia
56 along the Hellenic and Cyprus trenches (Dewey & Şengör, 1979; Taymaz et al., 1991; Taymaz
57 et al., 2007; Schildgen et al., 2014). GPS measurements (Reilinger et al., 2006) indicate that
58 slab rollback of the subducting African lithosphere could have a major effect on the rapid
59 deformation of Anatolia. The NAFZ, a right-lateral (dextral) fault system of Miocene age,
60 forms the boundary between the Anatolian plate to the south and the Eurasian plate to the north
61 (Barka, 1992; Le Pichon et al., 2015; Şengör et al., 2005). It stretches over 1600 km across

62 Anatolia (Figure 1) and has generated several destructive earthquakes in the 20th century

63 (Şengör et al., 2005).

64 The present work aims to elucidate the origin of seismic velocity contrasts in the crust and

65 uppermost mantle along the central NAFZ using joint inversion of P-receiver functions and P-

66 wave polarisation data. Several suture zones and tectonic boundaries are located across

67 Anatolia, bearing witness of the complex tectonic history involving successive accretion and

68 collision events, i.e., the Intra-Pontide and Izmir-Ankara-Erzincan Suture Zones (IAESZ), the

69 Istanbul Zone, the Sakarya Zone, the Central Pontides, the Kırşehir Massif, the Ezine Pazari-

70 Sungurlu Fault and the Çankırı Basin (Kaymakçı et al., 2009, 2003) (Figure 1). The Pontides

71 in the north of the study area belong to the Sakarya Continent terrane. The Kırşehir Block, as

72 the northern continuation of the metamorphic Anatolides, is located to the south of the study

73 area (Şengör and Yılmaz, 1981). The Çankırı Basin lies above the east-west trending IAESZ

74 between the Pontides to the north and the Kırşehir Block to the south (Kaymakçı et al., 2003)

75 (Figure 1). Kaymakçı (2000) propose that the Çankırı Basin was formed from Late Cretaceous

76 to Early Miocene times in response to the collision and indentation of the Sakarya Continent

77 and the Kırşehir Block. The sedimentary infill of this basin has a thickness of more than 4 km,

78 with sediment ages ranging from Late Cretaceous to present. Information on the crustal seismic

79 velocity structure across this region will provide new insight into the distribution of the

80 different crustal blocks and weak zones at depth, and their possible link to seismicity along the

81 NAFZ.

82

83 **2. Previous seismological work**

84 The NAFZ has been subject to several seismic experiments, the data from which have been

85 analysed using a variety of methods. In the early 2000s, relationships between seismicity and

86 crustal velocity structure beneath the NAFZ were investigated by local earthquake tomography

87 (Nakamura et al., 2002; Yolsal-Çevikbilen et al., 2012; Polat et al., 2016; Çubuk-Sabuncu et

88 al., 2017) and active-source seismic tomography (e.g. Karabulut et al., 2003; Bayrakci et al.,

89 2013) in the Marmara Sea region. Gans et al. (2009) interpreted regional Pn velocity anomalies

90 as evidence for slab break-off under Anatolia. Koulakov et al. (2010) presented a regional

91 tomography model showing that the crust in the western NAFZ is characterised by low Vp and

92 Vs, and high Vp/Vs ratios. Recently, full-waveform tomography of the crust in western

93 Anatolia by Çubuk-Sabuncu et al. (2017) confirmed these results. Seismic activity, as an

94   indicator of ongoing deformation within the crust, has been shown to occur not only along the
95   main branch of the NAFZ but also to extend to the south. (see Taymaz et al., 2007a for the
96   2000 Orta earthquake, Çubuk-Sabuncu et al., 2014 for the 2005 and 2008 Bala-Sırapınar
97   earthquakes; Karasözen et al., 2013)

98   In the last decade, two dense temporary seismic arrays were deployed across the western and
99   central NAFZ. These new stations allowed for local high-resolution seismic analyses and
100   expanded the data coverage for regional seismological models. Yolsal-Çevikbilen et al. (2012)
101   imaged small-scale Vp/Vs variations in the crust of the central NAFZ and identified high-
102   velocity blocks in the mid to lower crust that appear to be dissected by suture zones. Using
103   ambient noise tomography, Warren et al. (2013) imaged the crust of central and eastern
104   Anatolia. They found that most crustal velocity variations could be attributed to tectonic
105   boundaries and suture zones. However, they did not detect robust correlations between
106   velocities and the NAFZ, consistent with the results of Yolsal-Çevikbilen et al. (2012). The
107   receiver function results of Kahraman et al. (2015) do not show evidence of large Moho
108   variations in response to the western NAFZ, but they contain signals indicative of rheological
109   differences across the fault zone reaching into the upper mantle. In contrast, autocorrelation of
110   ambient seismic noise suggests a substantial Moho offset related to the northern branch of the
111   NAFZ in the same region, while no such offset is observed on the southern branch (Taylor et
112   al., 2016). Polat et al. (2016) carried out local P- and S-wave tomography to image 3D seismic
113   velocity variations across different branches of the NAFZ in the Marmara Sea region. They
114   found that high-velocity anomalies appear to be coincident with the rupturing segments of the
115   NAFZ where most of the observed high seismicity is concentrated. Papaleo et al. (2018, 2017)
116   imaged the lithosphere of the western NAFZ using teleseismic tomography and identified
117   substantial P- and S-velocity variations along- as well as across-strike the various branches of
118   the NAFZ. Licciardi et al., 2018 investigated the anisotropy in the central NAFZ based on
119   azimuthal variations of receiver functions and found that the NAFZ divides a crustal block of
120   relatively weak and homogeneously oriented anisotropy to the north from a highly and
121   heterogeneously anisotropic block to the south, with the strongest anisotropy in the upper 15
122   km of the crust.

123   A number of regional-scale seismic studies have been carried out with combined datasets from
124   nationwide networks of permanent stations and local temporary arrays. Here we briefly discuss
125   three of these studies whose results are relevant to this work. Firstly, a recent full-waveform
126   tomography study was performed over the entire Anatolian plate by Fichtner et al. (2013a,b).
127   Their results suggest that Vs structure in the mid/lower crust and uppermost mantle correlates

128 with both the NAFZ and suture zones in the region. These authors interpreted the NAFZ as a
129 Tethyan suture zone representing a transition from a broad zone of weakness in the upper
130 mantle to a narrower focussed deformation zone in the rigid blocks of the crust. Secondly,
131 Moho depths beneath the entire Anatolian plate were obtained from receiver function analysis
132 by Vanacore et al. (2013). Their model implies that small-scale fragments of thinned crust (i.e.,
133 shallow Moho) appear to be dissected by the NAFZ. Thirdly, a regional ambient noise
134 tomography by Delph et al. (2015) inferred a clear relationship between suture zones and
135 velocity anomalies across Anatolia, but only a weak link between the NAFZ and velocity
136 anomalies.

137 Though these previous seismic studies have provided important insight into the interplay
138 between lithospheric structure and the NAFZ, they have not yet succeeded in providing a
139 coherent picture of how the deformation is distributed with depth along the entire fault. This
140 may be due to the fact that different methods have inherently varying sensitivities and
141 resolutions that produce contrasting images of the same general crust-upper mantle structure
142 along the NAFZ. Alternatively, the structural variations are real and reflect differences in
143 rheological properties and style of deformation along the fault zone. We shall contribute new
144 insight to this critical discussion by applying a novel joint inversion of P-receiver functions
145 and P-wave polarisation to a large natural-source seismic dataset collected across the central
146 NAFZ.

147

148 **3. Data**
149 In the present study we analysed three-component teleseismic waveform data extracted from
150 continuous recordings that were acquired between January 2006 and May 2008 at 38 broadband
151 seismic stations within the framework of the North Anatolian Fault (*NAF*) passive seismic
152 experiment (Biryol et al., 2010). For each station, we selected the events with high signal-to-
153 noise ratio waveforms using a visual inspection process. These waveforms were extracted from
154 a list of about 1000 teleseismic events with magnitudes ≥ 5.5 that occurred at epicentral
155 distances (Δ) between 30° and 100°. Most of the events originate from the first quadrant for
156 the selected Δ range, corresponding to the major circum-Pacific seismogenic zones (Figure 2).
157 Additionally, we used similar teleseismic data from 14 stations belonging to different seismic
158 networks deployed in the study area (see Table 1) – these data were downloaded through
159 *ORFEUS* (http://www.orfeus-eu.org/). Eleven other stations from *ORFEUS*, as well as station

160　*DOGL* of the *NAF* were disregarded due to incomplete waveforms, poor data quality or
161　apparent timing problems. Station *DOGL* recorded a sufficient number of good events, but the
162　signals lack P-wave energy on the radial component (no significant signal at 0 sec in the R-
163　receiver function) (see Supplementary File S1). The absence of P-wave energy on the radial
164　component of a seismogram indicates a near-vertical apparent incident angle that translates
165　into unrealistically low apparent velocities. *DOGL* is located directly atop the ESF, where
166　strong scattering and boundary effects, as well as heavily fractured bedrock are expected and
167　may obscure the signal. As we do not have additional information that could help mitigate this
168　peculiar behaviour at *DOGL*, we decided to disregard the station entirely. The spatial
169　distribution of the 51 stations ultimately used in our analysis is shown in Figure 1. An overview
170　of station names, locations, network and number of processed events for all these stations can
171　be found in Table 1. Further details about the earthquakes used in this study are provided in
172　Supplementary File S2.

173

174　**4. Receiver function and Vs$_{app}$ inversion**
175　Our inversion method employs two data sources as inputs: P-receiver functions and P-wave
176　polarisations. The first data source, P-receiver functions (RFs), provide estimates of the
177　grounds' impulse response by deconvolving the incident wavefield from the converted
178　wavefield (Rondenay, 2009). Here, we generate receiver functions by applying water-level
179　deconvolution (Ammon, 1991; Clayton and Wiggins, 1976; Langston, 1979) to the waveforms
180　of recorded P-to-S (Ps) converted teleseismic earthquakes. On its own, RF inversion is already
181　a widely-used and well-established technique to obtain quantitative information on the
182　lithospheric velocity structure from these deconvolved conversions (Owens et al., 1987;
183　Ammon et al., 1990; Cassidy & Ellis, 1993; Sandvol et al., 1998; Darbyshire, 2003; Ottemöller
184　& Midzi, 2003). The second data source, the polarisation of incident P-waves, provides insight
185　into the absolute S-wave velocity distribution in the shallow subsurface within a homogeneous
186　medium (Wiechert and Zoeppritz, 1907). This P-wave polarisation information is contained in
187　the ratio of the radial (R) to the vertical (Z) RFs, i.e., R-RF/Z-RF, at zero delay time
188　(Svenningsen & Jacobsen, 2007). If the velocity changes with depth, then the polarisation now
189　reflects an apparent S-wave velocity (*Vs$_{app}$*), which integrates the velocities over the entire
190　depth range covered by the dominant wavelength of the signal. A set of apparent S-wave
191　velocities computed from different wavelengths can then be inverted to recover the absolute

192   velocity model. Here, we estimate the vertical apparent S-wave velocity distribution by

193   computing the R-RF/Z-RF ratio at increasing periods (T), following the procedure by

194   Svenningsen & Jacobsen (2007). This principle has recently been applied to both onshore and

195   offshore studies (Chong et al., 2018; Hannemann et al., 2016; Schiffer et al., 2016, 2015). Each

196   individual RF is used to calculate distinct $Vs_{app}(T)$ curves, while the median curve is considered

197   to give the most robust representation. T is defined as 26 values on a logarithmic scale from 1

198   to 25 sec. The data error is defined as the standard deviation of the 68% $Vs_{app}(T)$-curves closest

199   to the mean.

200   We jointly invert Vs_{app} curves and RF waveforms using a linearised inverse procedure (Ammon

201   et al., 1990; Menke, 1989; Tarantola and Valette, 1982) based on to the approaches presented

202   in Schiffer et al., (2015) and Schiffer et al. (2016). The RFs are modelled from -1 to 20 sec

203   delay time and Vs_{app} from 0 to 25 sec periods. The non-uniqueness of the inverse problem is

204   reduced by parameterising layers in delay-time instead of thickness (Jacobsen and

205   Svenningsen, 2008). The inversion is adjusted to primarily fit the $Vs_{app}(T)$ curves by weighting

206   these by a factor of 2 compared to the RF waveforms. The inclusion of RF waveforms in the

207   inversion helps retaining the sensitivity to sharp velocity discontinuities, which is otherwise

208   lost when only inverting $Vs_{app}(T)$. Vp values were determined on the basis of Poisson's ratios

209   between 0.25 and 0.3 for various lithologies (Christensen, 1996) and densities are calculated

210   from Vp at different depth (Christensen and Mooney, 1995). The inversion is thereby not

211   technically inverting for Vp as an independent quantity, but the best fitting Vs-Vp combination

212   is estimated following the predefined lithology-dependent Vp/Vs ratios. We can therefore use

213   the resulting Vp/Vs ratios for interpretation. *A priori* data errors based on the independent data

214   covariance matrices are used to automatically weigh the individual datasets. That is, if one

215   dataset shows a larger spread, the observed error is large and the weight of the respective

216   dataset is reduced in the inversion. Data and model uncertainties are thoroughly discussed in

217   *Section 6.1*.

218   Figure 3 shows examples of RFs and Vs_{app} curves for two stations with different number of

219   events, for comparison – *ALIC* (Figure 3a) has a large number of events, whereas *KOZK*

220   (Figure 3b) has a smaller number of events. The reduced dataset at *KOZK* leads to a much

221   larger observed data error compared to *ALIC*. Corresponding figures from all other stations are

222   documented in Supplementary File S3. The Vs_{app}-method is only stable for frequencies

223   contained in the original recorded waveforms. Hence, in our case, the original waveforms must

224   contain frequencies down to at least T^{-1}=0.04 Hz (T=25 sec).

225   Examples of the progression of the inversion at these two stations are shown in Figure 4, and
226   corresponding figures for all other stations are shown in Supplementary File S4. Starting
227   models and observed data are represented by black lines, whereas each iteration of the
228   linearised inverse model is colour coded with blue-green-yellow-orange-red colours
229   representing early-to-late iterations and the last iteration is always denoted in red. The bottom
230   left panel shows the evolution of the data error though the various iterations. The error is
231   usually reduced at each iteration of the inversion, which ends when the models and errors
232   converge, i.e. changes of less than 1% are observed for more than 2 iterations (see details in
233   the figure caption). The starting models comprise three major discontinuities at mid-crustal and
234   Moho depths to reflect the largest peaks observed in the RFs, and an additional layer boundary
235   in the upper mantle to allow for sub-Moho structure. Three thin layers with 0.2, 0.3 and 0.5 sec
236   delay time are also defined at the top of the model to adequately constrain sedimentary basins.
237   The uppermost velocities of the starting model are set to fulfil the first three values of the
238    $Vs_{app}(T)$ curves, respectively. Velocities and depths/delay times are virtually unconstrained in
239   the inversion, meaning that both model parameters can freely change without causing a large
240   model error. There are two exceptions to this rule: (1) the uppermost S-wave velocity, which
241   is more tightly constrained to the first Vs_{app}(T=1 sec) by an *a priori* standard deviation of 0.2
242   km/s; and (2) the lowermost mantle half-space velocity, which is tied to a velocity of Vs=4.6
243   km/s by an *a priori* model error of 0.2 km/s. The final model is defined by the average of the
244   last 10 model iterations.

245   We perform a number of synthetic tests to evaluate the performance of the inversion. A detailed
246   description and documentation of the different model setups, the progression of the inversions
247   and inversion results are shown in Supplementary File S5. We define four hypothetical crustal
248   reference models on top of a mantle half space: (i) A two-layered crystalline crust (20 km of
249   upper and lower crust), (ii) the same model with the addition of two sedimentary layers of 1.5
250   and 3.5 km thickness replacing the uppermost crystalline crust, (iii) the same model as (i) with
251   a 5 km thick high velocity lower crustal layer and, finally, (iv) the combination of models (ii)
252   and (iii) with two sedimentary layers and high velocity lower crust. We use the same ray
253   geometries as those for the events recorded at station *ALIC*, taking into account variations in
254   ray-parameters and associated changes in P-wave amplitude at t=0 sec and the delay times of
255   primary and multiple conversions. We apply exactly the same inverse algorithm as that
256   described above in this section to the synthetic data, without any *a priori* model information.
257   Four tests are performed for each of the reference models. (a) An average of 1% random

258 velocity and layer depth perturbations are added to the velocity model before calculating each

259 the 47 synthetic waveforms. This allows us to approximate the effects of ambient geological

260 changes in the vicinity of the station. (b) The same setup as for (a), with the addition of realistic

261 seismic noise captured in a random time window preceding the P-arrivals in the real data

262 recorded at station *ALIC*. (c) The same test as described in (a) with 5% model perturbations.

263 (d) The same test as described in (c) with additional noise from the observed receiver function.

264 We perform 4 additional tests to explore the role of velocities in the starting models: The

265 structurally most complex models with most and least perturbation and noise are inverted with

266 a constant mantle velocity; another is performed with a constant crustal velocity on top of the

267 mantle half space.

268 In all tests, the crustal velocity structure is well recovered. However, the data and recovered

269 velocity models show larger misfits with added noise and increasing geological variation, as is

270 to be expected. Geological variations appear to create smoother primary conversions and even

271 smoother multiple conversions, which replicate apparent velocity gradients rather than sharp

272 discontinuities. Because of the intentional minimal setup of our models, these apparent

273 gradients cannot be fully recovered. However, it can be observed that the interfaces are

274 modelled using a step if the model setup allows for such structure and an additional layer is

275 available, e.g. for the Moho and other known interfaces. In summary, our synthetic tests reveal

276 that the overall model recovery is very good despite the presence geological variations and

277 noise, and that our inverse approach can thus be deemed robust.

278 **5. Results**

279 The final inversion results for the stations that we have used as examples in *Section 4*, *ALIC*

280 and *KOZK*, are shown in Figure 5. Those for all other stations are presented in Supplementary

281 File S6. The 1D model results are integrated and displayed as maps showing average Vs over

282 the 0-5 km and 5-15 km depth ranges, and average Vp/Vs ratio in the top 15 km of the study

283 area (*Section 5.1*, Figure 6-7). All maps are produced using kriging of every individual station

284 results using the MATLAB kriging toolbox, DACE (Lophaven et al., 2002). In the rest of the

285 section, we interpret the Vs models in terms of (i) thickness of the sedimentary cover (*Section*

286 *5.2*), (ii) depth to crystalline basement (excluding metasediments) (*Section 5.2*), and (iii) depth

287 to Moho (*Section 4.3*). These three interfaces are defined according to velocity discontinuities

288 that exceed certain thresholds in Vs. The sedimentary thickness is defined by the shallowest

289 discontinuity that exceeds Vs=2.5 km/s. The depth to the crystalline basement interface is

290   defined as the shallowest discontinuity at which Vs=3.05 km/s is exceeded. Basement depth is
291   different from the sedimentary thickness, as we assume that possible metasediments are not
292   part of the sedimentary succession, while basement depth does include these. The Moho is
293   defined as the average depth of all model-discontinuities that lie in the range of Vs from 4.05
294   to 4.6 km/s.

295   To put our inversion results in a regional context, we display them in map view in Figure 8 and
296   along five N-S oriented profiles in Figure 9. And to link back to the input data, Figure 10
297   displays the receiver function waveforms on the same five profiles, along with the interpreted
298   interfaces from Figure 9. It is usually difficult to identify clear phases for the sedimentary layers
299   and basement interface in the receiver functions of Figure 10, as these signals interact with the
300   primary P-wave and sedimentary multiples, and form complex interferences. For most stations,
301   the interpreted Moho corresponds to a clear positive pulse in the receiver functions. However,
302   at a few stations the Moho signal is either weak or absent. This deterioration of the Moho signal
303   likely stems from destructive interference with sedimentary multiples. This effect might be
304   amplified when the Moho is gradational or characterised by a small velocity discontinuity, for
305   example when a high-velocity lower crust is present.

306   We are aware of the uncertainties of the inverse approach and the fact that different lithologies
307   can have overlapping velocities. In particular, fracturing of crystalline rocks can reduce S-wave
308   velocities to values approaching those of sediments, an effect that may be important in a highly
309   deformed study area such as the NAFZ. Additionally, seismic anisotropy related to fracturing,
310   strike-slip deformation, metamorphism or intrusions may have a large impact on the measured
311   velocities, depending on the primary orientation of incoming earthquake waves (Fouch and
312   Rondenay, 2006). This may lead to errors in the interpretation.

313

314   *5.1 Crustal velocity structure*
315   Clear variations in Vs can be observed in the 0-5 km depth range (Figure 6a). Three areas of
316   consistently high or low velocities are identified: (i) In the Çankırı Basin and Kırşehir Block,
317   the uppermost Vs are generally low (1.9-2.2 km/s), with few exceptions (*CORM, YOZ*); (ii) the
318   northwest of the study area (Istanbul Zone and Central Pontides, ~41.5ºN, ~32.5-34.5ºE)
319   exhibits higher Vs (2.7-3.1 km/s); and (iii) the area between NAFZ/ESF and the IAESZ, in the
320   central-eastern part of the study area, also exhibits higher Vs (stations *KUZA, BAGB, TOKT,*
321   *YESI*). All other areas have moderate Vs variations (~2.2-2.7 km/s) on smaller scale (small

322 wavelength), which may reflect the natural geological variation in the study area including
323 minor undulating basins and transitions between different terranes or levels of fracturing and
324 faulting. The velocity variation in the 0-5 km depth range is particularly indicative of the
325 presence or absence of sedimentary layers. For example, the Çankırı Basin is clearly outlined
326 by low velocities (Figure 6a). Conversely, high Vs represent areas without significant
327 sedimentary cover and basement highs, such as the Istanbul Zone and the Central Pontides.

328 Vs in the 5-15 km depth range may still be affected by very deep sedimentary basins, but mainly
329 represent variations in seismic properties, compositions and fabrics of the upper-middle
330 crystalline crust (Figure 6b). The lateral distribution of Vs between 5-15 km depth shows
331 variations at much larger wavelength compared to the shallow layers. The Çankırı Basin and
332 Kırşehir Massif are still characterised by relatively low Vs (2.5-3 km/s), which may indicate
333 the presence of deep basin structure (>5 km) beneath the Çankırı Basin, and the presence of
334 metasediments in the Kırşehir Massif. All other areas are characterised by Vs of >3 km/s, with
335 the exception of a few isolated stations (*KVT, SVSK, KUZO*).

336 The Vp/Vs ratios across the study area show clear variations ranging from approximately 1.73
337 to 1.85 (Figure 7). High Vp/Vs ratios are observed in the Çankırı Basin, in the southeast of the
338 study area and at a few stations located above the NAFZ. Low values are found for areas of
339 high topography and no or little sedimentary cover, in the northwest (Istanbul Zone), central
340 north (Central Pontides) and central west (Sakarya Zone and the area bound by the IAEFZ and
341 NAFZ). Though we shall further discuss these results in the next sections, we must remind the
342 reader that they have some limitations, as Vp is not a proper inversion parameter. Instead,
343 Vp/Vs ratios are defined as a function of Vs. Still, the inversion estimates the optimal Vs-Vp
344 combination as a function of depth beneath each station.

345

346 *5.2 Sedimentary thickness and basement depth*
347 The interpreted sedimentary thickness (Figure 8a) roughly mimics the map of Vs in the 0-5 km
348 depth range (Figure 6a). The deepest and largest basin is estimated in the area of the Çankırı
349 Basin (stations *CANT, PANC, KARG, CAYA, CRLU*), with up to 6 km of sedimentary rocks.
350 Another deep but spatially quite confined basin is inferred above and to the north of the NAFZ
351 in the western part of the study area (stations *KUZO* and *ALIN*). Another small area of thicker
352 sedimentary cover is found around station *OGUR* located on top of the NAFZ in the centre of
353 the study area. Thin sedimentary cover (< 1km) is inferred across the northwest (Istanbul

354 Zone), central-north (Central Pontides) and southeast regions of the study area, whilst all other
355 areas indicate moderate thicknesses of 1-3 km.

356 The depth to crystalline basement map (Figure 8b) shows a slightly different pattern compared
357 to the sedimentary thicknesses (Figure 8a). Crystalline basement generally lies deep (>8 km)
358 in most of the Çankırı Basin (*CUKU, CANT, KARG, PANC, CRLU, GOCE, KOZK*), but some
359 stations indicate shallower basement (~5 km at *CAYA* and *CORM*). In the southern part of the
360 Çankırı Basin, the sedimentary layer has been estimated to be only 1-3 km thick at locations
361 where the basement is >8 km deep (*CRLU, GOCE, KOZK*), suggesting that a 5-7 km thick
362 metasedimentary layer or heavily fractured uppermost crystalline crust may exist beneath this
363 region. This also applies to a group of stations close to the NAFZ in the west of the study area
364 (*SEYH, INCE*) and in the southeast of the study area (*KIZI, SVSK*), where thinner sedimentary
365 successions coincide with deep crystalline basement. In most other areas, deep basement
366 generally coincides well with thick sedimentary basins, or *vice versa*, though the general
367 character of the depth to basement map appears much smoother than the map of sedimentary
368 thickness (Figure 8a).

369 *5.3 Moho depth*
370 The Moho is shallow beneath the Çankırı Basin (34-36 km) and deepens abruptly to the north
371 to reach its greatest depth beneath the Central Pontides (40-42 km) (Figure 8c). Locally very
372 shallow Moho is inferred beneath stations *KUZO* and *SEYH* in the central-western part of the
373 study area that straddles the NAFZ. Another moderate Moho shallowing is reported at station
374 *SVSK* in the southeast. The Moho is observed at intermediate depths (~35-38 km) elsewhere
375 across the study area (Figure 8c). The Moho depth negatively correlates with the sedimentary
376 thickness and depth to basement maps in most areas, i.e. shallow Moho correlates with thick
377 sedimentary successions and *vice versa*. This relationship is limited by the different
378 wavelength-character of the interfaces (base of sedimentary basins, top of crystalline basement
379 and the Moho). For example, some stations in the Çankırı Basin (CAYA, CORM) and in the
380 east of the study area (BOKE, KUZA, TOKT, KIZI, SVSK, KVT, ARSL) do not show this
381 negative correlation.

382

383 *5.4 Regional characterisation*
384 To further illustrate large-scale variations in geophysical properties across the region, we
385 subdivide the study area into four domains of distinct overall seismic structure, as evaluated

386 from the maps in Figure 6-8. These domains are roughly delimited by major suture zones and
387 are defined as follows (see Figure 11a): (I) the Istanbul Zone in the northwest, (II) the Eastern
388 Sakarya Zone in the north-east, including the Central and Eastern Pontides (III) the Western
389 Sakarya Zone in the south-west, and (IV) the Çankırı Basin and Kırşehir Massif in the south-
390 east. The seismic properties and structures are averaged for all stations within each of the
391 domains and plotted in Figure 11b. A number of interesting patterns emerge from this
392 integrated view. For example, we find that domains I and II show much higher Vs values for
393 the upper 5 km (>2.5 km/s) and 5-15 km depth (>3.2 km/s) compared to regions III and IV
394 (<2.35 km/s and <3.1 km/s in the two depth ranges). This is also reflected in the thickness of
395 the sedimentary layer, which is thinnest in domain II (~1.5 km), followed by domain I (~2.0
396 km), compared to an average sedimentary thickness of >2.5 km in domains III and IV. The
397 Moho is deepest in domain II with an average of almost 40 km, intermediate in domain I (~37.5
398 km) and thinnest in domains III and IV (~36 km). Domains II and IV, which together cover the
399 central to eastern portion of our study area, exhibit the most extreme contrast in seismic
400 structure. Domain II has the highest seismic velocities, the thinnest sedimentary layers and the
401 deepest Moho, whereas domain IV is characterised by the lowest velocities, the thickness
402 sedimentary layers and shallowest Moho (together with domain III). These relationships can
403 also be directly assessed by comparing the average RF waveforms from each domain (Figure
404 11c). The average RFs from domains I and II show the highest amplitudes for the incident P-
405 wave (t=0 sec), indicative of high uppermost velocities. By contrast, the P-wave amplitudes
406 are considerably lower for domains III and IV, indicating low uppermost crustal velocities.
407 This is reflected in the average Vs_{app} curves (Figure 11d), which are lowest for domain IV,
408 followed by domain III and similarly high for domains I and II. Domains I, III and IV have
409 very similar values of average Vs_{app} at periods T>4 sec, while region II clearly has higher
410 velocities at these levels. At T>20 sec, velocities lie in a similar range for all domains. The
411 average models and interface interpretations are shown in Figure 11e.

412

6. Discussion

414 We derived a crustal model of the central NAFZ using a novel inversion of P-receiver function
415 and P-wave polarisation data extracted from teleseismic waveform recorded at 51 broadband
416 stations. In this section, we discuss our recovered upper-crustal shear-wave velocity structure

417   in light of the tectonic history of the region, known surface expressions of major tectonic

418   boundaries and fault zones, and the distribution of local earthquakes.

6.1 Model Uncertainties

420   Before we discuss the tectonic implications suggested by our inverse modelling, we will

421   describe and discuss the model and data uncertainties. The inversion algorithm uses *a priori*

422   data and model uncertainties (see Section 4). While the data uncertainties are taken directly

423   from the standard deviations of the observed data, the model perturbations are loosely

424   constrained allowing the model to be completely data driven (with exception of the uppermost

425   layer velocity and the lowermost mantle velocity, see Section 4). One output of the inversion

426   is the *a posteriori* covariance matrix consisting of uncertainties for each model parameter from

427   which we derive our model uncertainty estimates (e.g. Tarantola & Valette, 1982; Schiffer et

428   al., 2016, 2015). The model uncertainties are illustrated in each individual model result as grey

429   shaded areas underlying the velocity models in Figure 5a and Supplementary File S6. The *a*

430   *priori* data uncertainties, as well as the three major interpreted discontinuities (sedimentary

431   thickness, depth of basement, Moho depth – converted to delay times) and their *a posteriori*

432   uncertainties, are all shown in Figures 12 (receiver functions) and 13 (Vs_{app} curves). This

433   provides an overview for all stations of the relative quality of the data and modelling results,

434   and gives a regional context to these quality attributes. Clearly, some stations yield better/more

435   consistent data than others, which is reflected in smaller data uncertainties (grey shaded areas

436   around receiver functions and Vs_{app} curves in Figures 12 and 13). There is no identifiable

437   regional pattern of larger or lower data uncertainties of the receiver functions. Examples of

438   stations with larger receiver function uncertainties include ALIN, ARSL, CANT, ILGA,

439   KOZK, KVT, PANC, POL, SEYH, SVSK. As a result, these stations usually exhibit larger

440   uncertainties in the estimates of the interpreted interfaces and layers (sedimentary basins, depth

441   to basement and Moho, Figure 12). The large uncertainties in the receiver functions waveforms

442   are also reflected in a wider distribution of the Vs_{app} curves (Figure 13), but not always.

443   Reciprocally, large uncertainties in Vs_{app} do frequently, but not always, coincide with larger

444   error bars in the receiver functions. Regionally, the Vs_{app} uncertainties seem to show a spatial

445   pattern: stations in areas within sedimentary basins (blue and magenta) generally have larger

446   uncertainties than those stations in areas with very shallow basement (red and cyan).

447   We also document the uncertainty measures on a set of maps displaying the average errors for

448   Vs and layer depths for each station, as well as the root-mean-square (RMS) data misfit

449   weighted and normalised with the inverse *a priori* data uncertainties (see Supplementary File

450 S7). The latter penalises the RMS based on data uncertainties, meaning lower RMS when the
451 data uncertainty is high, and *vice versa*. For the models, we find that most S-wave velocity
452 errors are of the order of ~0.1-0.15 km/s and that most depth errors are scattered around a value
453 of 0.5-1 km. The weighted and normalised data misfits show usual values of 0.05-0.2. We do
454 not observe any clear geographical correlation between the distribution high/low model
455 uncertainties and data misfits. Instead, very high/low model uncertainties and data misfits seem
456 to be randomly distributed and do not appear to coincide with one another (Supplementary File
457 S7).

458 Although our means of estimating uncertainties is formally rooted in the theory of the inverse
459 problem, it appears that these uncertainties are somewhat underestimated. Indeed, the resulting
460 depth and velocity errors appear too low to represent realistic model uncertainties. A common
461 approach to achieve more realistic uncertainties is employing random sampling approaches
462 (e.g. Monte Carlo or Bayesian techniques). However, our inverse algorithm is not currently
463 implemented to apply these approaches, which is why we used the theoretical method described
464 above.

465 *6.2 The depth extent of the NAFZ*

466 Localised shear deformation along the continental strike-slip fault system of the NAFZ is
467 regarded as the primary source of seismic hazard in the region. Local earthquake clusters have
468 been detected along various segments of the NAFZ, with seismicity generally focussed in the
469 upper 15 km of the crust (Bohnhoff et al., 2016; Bulut et al., 2009; Poyraz et al., 2015; Taymaz
470 et al., 2001). Accurate earthquake locations and earthquake cluster geometries are crucial
471 information for understanding strain accumulation during the earthquake cycle and the
472 assessment of seismic hazard, but are not well resolved at mid- to lower-crustal depths. Hence,
473 a highly debated question is how far strike-slip deformation extends at depth.

474 Our results from the central NAFZ indicate a strong correlation of the entire crustal velocity
475 structure with surface expressions of faults and terrane boundaries. The NAFZ appears to form
476 a boundary between two regions of differing crustal characteristics, based on both crustal
477 velocity distributions (Figure 6) and interpreted Moho depth (Figure 8,9): (1) a northern region
478 where crustal attributes vary over large wavelengths, with thick crust under the Central
479 Pontides and intermediate crust elsewhere; (2) a southern region where crustal attributes vary
480 over shorter wavelengths, with small-scale basins and basement highs. These observations are
481 better explained by focused deformation in the crust (more rigid behaviour), rather than by a

482 broader depth-distributed deformation pattern (more ductile behaviour). In their recent S-wave
483 tomography, Papaleo et al. (2018) have also reported focused deformation for a northwestern
484 segment of the NAFZ, with a width of ~10 km at upper crustal depths that widens to ~30 km
485 at lower crustal depths. Focussed deformation in the upper crust is also consistent with the
486 strong radial anisotropy ($V_{SV} > V_{SH}$) that has been measured close to the NAFZ down to 20-25
487 km depth (Çubuk-Sabuncu et al., 2017). Such seismic anisotropy may develop from
488 reorientation of rock fabrics during deformation, especially along strike slip faults (Storti et al.,
489 2003). Similarly, local shear wave splitting and converted wave analyses along the western and
490 central part of the NAFZ imply strong anisotropy related to major faults at depths of down to
491 15-20 km, often asymmetrically distributed with regards on both sides of the fault (e.g. Peng
492 & Ben-Zion, 2004; Hurd & Bohnhoff, 2012; Eken et al., 2013a; Liccardi et al., 2018).

493 Looking deeper into the lithosphere under the NAFZ, some tomographic results based on
494 inversion of teleseismic P-waves (Biryol et al., 2011) and full waveforms (Fichtner et al.,
495 2013a,b) indicate a sharp velocity contrast across the NAFZ reaching down to 100-150 km
496 depth. In contrast, results from Rayleigh wave tomography could not detect any significant
497 velocity changes across the NAFZ within the mantle lithosphere (Salaün et al., 2012). A
498 comprehensive shear-wave splitting study across the region indicates that there is a systematic
499 obliquity between the crustal and mantle anisotropy beneath the NAFZ (Paul et al., 2014),
500 further suggesting that NAFZ deformation is limited to the crust and decoupled from the
501 mantle. This behaviour is different from observations in northeast Tibet, where fast anisotropy
502 directions are nearly parallel to the strike of the North and South Kunlun faults, indicating a
503 vertically coherent deformation transmitted within the entire lithosphere (Eken et al., 2013b;
504 León Soto et al., 2012).

505 In summary, we find that deformation along the central NAFZ appears to be focussed in the
506 crust, which is consistent with a number of previous studies. However, seismic observations of
507 the lithospheric mantle are inconsistent with regards to how (or if) NAFZ deformation extends
508 to greater depths. Hence, the issue of how strike-slip deformation is manifested in the mantle
509 remains unresolved.

510

511 *6.3 Lithological Contrasts*
512 Şengör et al. (2005) have previously discussed a possible asymmetric distribution of elastic
513 properties across the NAFZ by identifying lithological contrasts produced by lateral

514   displacement along the NAFZ. Such lithological contrasts have been previously imaged across

515   the region by 3-D seismic tomography (e.g. Yolsal-Çevikbilen et al., 2012; Fichtner et al.,

516   2013a; Fichtner et al., 2013b; Delph et al., 2015; Çubuk-Sabuncu et al., 2017), fault-guided

517   head wave analyses (Bulut et al., 2012; Najdahmadi et al., 2016) and 2D/3D geoelectric

518   methods (Kaya et al., 2013). Our results show that the fault zones (most notably the NAFZ)

519   seem to accommodate rough, small-wavelength velocity perturbations indicative of small

520   basins and basement highs distributed in the vicinity of the fault line. These small-wavelength

521   variations extend down to the Moho but appear to be concentrated at basin and basement

522   depths. The character of the velocity structure appears to become smoother away from the

523   faults. In contrast, we observe that the suture zones crossing the study area strongly correlate

524   with larger-scale velocity variations and crustal structure inferred from the maps in Figures 6-

525   8 and the profiles in Figure 9. In particular, the IAESZ provides a clear outline to the velocity

526   structures marking the Çankırı Basin. Suture zones between different accreted terranes often

527   mark boundaries between different lithologies and compositions and this is clearly illuminated

528   by our seismic inversion. Subdividing the study area into several zones based on similar seismic

529   and crustal characteristics, as we have done in Section 5.4, reflects the strong segmentation of

530   the study area by the major tectonic boundaries and implies a dominant control of the tectonic

531   history on crustal structure (Figure 11).

532

6.4 Sedimentary infill

534   At regional scale, infill of sediments (both old and young) is most prominent and continuous

535   across the Çankırı Basin and parts of the Kırşehir Massif. Sedimentary and metasedimentary

536   layers have large thicknesses in the Çankırı Basin. The basement is deep in the southern and

537   eastern Kırşehir Massif, but only thin uppermost sediments are observed there, indicating a

538   thick metasedimentary succession.

539   At local scale, one would expect deformation and lateral offsets associated with major

540   transform fault systems to produce complex localised structures along the fault zones, including

541   small sedimentary basins. Our sedimentary thickness and depth to basement maps do indeed

542   show small-scale variations concentrated along the NAFZ, suggesting the existence of such

543   structures (small basins and basement highs) that are likely caused by deformation proximal to

544   the NAFZ.

545   A set of stations (*KUZO, SEYH*, and to some degree *ALIN, INCE*), which are located close to

546   the NAFZ at approximately 41°N, 33°W, exhibit large apparent sedimentary thicknesses

547   (*ALIN, KUZO*), deep basement (*KUZO, SEYH, ALIN, INCE*) and shallow Moho (*KUZO,*

548   *SEYH*). Though these observations may stem from real localised geological features, we must

549   also consider the possibility that they are artefacts caused by strong seismic anisotropy (see,

550   e.g., Licciardi et al., 2018) and/or complex scattering patterns from fractured/deformed rocks

551   or localised geological bodies along the NAFZ that act as point scatterers. A recent inversion

552   of coda wave envelopes in the same study area indicates that the effect of scattering attenuation

553   should be relatively small compared to the intrinsic attenuation (Gaebler et al., under review).

554   Thus, we can exclude scattering from the potential sources of artefacts. Further work beyond

555   the scope of this paper will be required to assess these effects.

556

557   *6.5 Crustal strength and seismicity along the fault*

558   An open question is how seismicity is distributed along fault zones. The NAFZ is related to

559   elevated seismic activity, which has included a number of damaging earthquakes (Bohnhoff et

560   al., 2016; Taymaz et al., 2001, 1991), but the factors that control the location and mechanism

561   of these earthquakes are not well understood. The occurrence of earthquakes maybe related to

562   a complex interplay between plate motions, the shape of the fault zone/plate boundary and

563   rheological variations in the lithosphere (Chester et al., 1993; Lyakhovsky et al., 2001). To see

564   whether our results can help address these questions, we propose to investigate the Vp/Vs ratio

565   of the upper 15 km of the crustal model (i.e., a measure of crustal weakness in the mostly brittle

566   part of the crust) in conjunction with the seismicity in the upper 20 km recorded since 2005

567   (Figure 7).

568   Although it is difficult to establish any robust correlation from the map in Figure 7, earthquakes

569   appear to cluster along the active faults and around regions of high Vp/Vs ratios (or possibly

570   at high Vp/Vs ratio gradients). Such high Vp/Vs ratios, if caused by high pore pressures and/or

571   water-filled microcracks (Gudmundsson, 1999; Zhao, 2015), could be associated with weak

572   zones that may accommodate deformation and seismic activity. Moreover, lateral variations of

573   high and low Vp/Vs ratio in the study area correlate well with the distribution of harmonic

574   energy values marking regions of strong anisotropy (Liccardi et al., 2018), which may be linked

575   to extensive dilatancy of fluid-filled microcracks within the top 15 km of the crust. Our results

576   suggest that, at least to some degree, the boundaries between weak and strong upper crustal

577 domains or the edges of weak zones (white areas in Figure 7) may focus deformation. We note

578 however that large parts of the study area lack sufficient station coverage to map crustal

579 properties well enough to draw additional conclusions. New seismic deployments are thus

580 needed to further test the hypothesised link between crustal boundaries and focused

581 deformation. The southwestern portion of the study area, which hosts a large earthquake cluster

582 centred at ~39.5°N, ~33°E, is a particularly attractive target for future deployments. Other

583 potential targets include earthquake clusters at ~40.5°N, ~33°E and at ~40.5°N, ~35°E.

584

585 **7. Conclusion**

586 Our novel joint inversion of P-receiver functions and P-wave polarisation provides estimates

587 of crustal velocity structure in the central NAFZ. We identify considerable velocity variations

588 (Vs=1.9-3.55 km/s) at upper crustal levels that correspond to known tectonic structures and

589 lineaments in the study area. Velocities in the uppermost 5 km outline the boundaries between

590 sedimentary basins (low velocities) and basement highs (high velocities). The most prominent

591 feature in this depth range is the Çankırı Basin, which is clearly outlined by the IAESZ. Smaller

592 basins are also inferred in vicinity to the NAFZ. Velocity contrasts in the 5-15 km depth range

593 mainly correspond to different crustal blocks. The IAESZ still appears as a major boundary at

594 these depths, separating areas of different crustal velocities. In particular, the Çankırı Basin

595 and the Kırşehir Massif are still well-visible. The NAFZ also seems to act as a large-scale

596 boundary between crustal blocks of differing elastic properties to the north and south of the

597 fault zone. These observations are reflected in our maps of crustal attributes (sedimentary

598 thickness, depth to basement, Moho depth) across the region. Our maps reveal that these crustal

599 attributes exhibit a rougher character (i.e., small-scale highs and lows) along the NAFZ

600 compared to regions away from the fault zone. Such small-scale variations are likely due to

601 localised deformation concentrated in the proximity of the NAFZ. The maps reinforce the

602 notion that the NAFZ represents a fundamental boundary in crustal properties between north

603 and south, with a sharp lateral contrast extending down to Moho depth. To the south of the

604 NAFZ, Moho depths variations occur over small scales, with several areas exhibiting local

605 highs and lows. In contrast, to the north, a single thick crustal block is observed in the central

606 part with intermediate Moho depth to the west and east. These results suggest that the NAFZ

607 is a feature that extends through the entire crustal column with relatively narrow/localised

608 deformation. Seismicity appears to cluster around areas of low Vp/Vs ratios, which are

609　interpreted as potential weak zones. Our results complement a wealth of previous geophysical,
610　geodetic and geological analyses that have been carried out across the NAFZ. Taken together,
611　all these results provide new insight into the relationships between crustal structure, tectonic
612　boundaries and seismicity. They help in expanding a vital geoscientific discussion whose
613　ultimate goal is the understanding of deformation, seismicity and associated seismic hazard in
614　the region.

615

631

632　**References**

633　Amante, C., Eakins, B.W., 2009. ETOPO1 1 arc-minute global relief model: Procedures, data sources
634　　　and analysis. NOAA Tech. Memo. NESDIS NGDC-24, National Geophysical Data Center,
635　　　NOAA. https://doi.org/doi:10.7289/V5C8276M
636　Ammon, C.J., 1991. The isolation of receiver effects from teleseismic P waveforms. Bull. Seismol. Soc.
637　　　Am. 81, 2504–2510.
638　Ammon, C.J., Randall, G.E., Zandt, G., 1990. On the nonuniqueness of receiver function inversions. J.
639　　　Geophys. Res. Solid Earth 95, 15303–15318. https://doi.org/10.1029/JB095iB10p15303
640　Barka, A.A., 1992. The north Anatolian fault zone. Ann. Tectonicae 6, 164–195.
641　Bayrakci, G., Laigle, M., Bécel, A., Hirn, A., Taymaz, T., Yolsal-Çevikbilen, S., Team, S., 2013. 3-D
642　　　sediment-basement tomography of the Northern Marmara trough by a dense OBS network
643　　　at the nodes of a grid of controlled source profiles along the North Anatolian fault. Geophys.
644　　　J. Int. 194, 1335–1357.

645 Biryol, C.B., Beck, S.L., Zandt, G., Özacar, A.A., 2011. Segmented African lithosphere beneath the
646   Anatolian region inferred from teleseismic P-wave tomography. Geophys. J. Int. 184, 1037–
647   1057.
648 Biryol, C.B., Zandt, G., Beck, S.L., Ozacar, A.A., Adiyaman, H.E., Gans, C.R., 2010. Shear wave splitting
649   along a nascent plate boundary: the North Anatolian Fault Zone. Geophys. J. Int. 181, 1201–
650   1213. https://doi.org/10.1111/j.1365-246X.2010.04576.x
651 Bohnhoff, M., Martínez-Garzón, P., Bulut, F., Stierle, E., Ben-Zion, Y., 2016. Maximum earthquake
652   magnitudes along different sections of the North Anatolian fault zone. Tectonophysics 674,
653   147–165. https://doi.org/10.1016/j.tecto.2016.02.028
654 Bulut, F., Bohnhoff, M., Eken, T., Janssen, C., Kılıç, T., Dresen, G., 2012. The East Anatolian Fault
655   Zone: Seismotectonic setting and spatiotemporal characteristics of seismicity based on
656   precise earthquake locations. J. Geophys. Res. Solid Earth 117, B07304.
657   https://doi.org/10.1029/2011JB008966
658 Bulut, F., Bohnhoff, M., Ellsworth, W.L., Aktar, M., Dresen, G., 2009. Microseismicity at the North
659   Anatolian fault in the Sea of Marmara offshore Istanbul, NW Turkey. J. Geophys. Res. Solid
660   Earth 114.
661 Bürgmann, R., Dresen, G., 2008. Rheology of the Lower Crust and Upper Mantle: Evidence from Rock
662   Mechanics, Geodesy, and Field Observations. Annu. Rev. Earth Planet. Sci. 36, 531–567.
663   https://doi.org/10.1146/annurev.earth.36.031207.124326
664 Cassidy, J.F., Ellis, R.M., 1993. S wave velocity structure of the northern cascadia subduction zone. J.
665   Geophys. Res. Solid Earth 98, 4407–4421. https://doi.org/10.1029/92JB02696
666 Chester, F.M., Evans, J.P., Biegel, R.L., 1993. Internal structure and weakening mechanisms of the
667   San Andreas fault. J. Geophys. Res. Solid Earth 98, 771–786.
668 Chong, J., Chu, R., Ni, S., Meng, Q., Guo, A., 2018. Receiver function HV ratio: a new measurement
669   for reducing non-uniqueness of receiver function waveform inversion. Geophys. J. Int. 212,
670   1475–1485. https://doi.org/10.1093/gji/ggx464
671 Christensen, N.I., 1996. Poisson's ratio and crustal seismology. J. Geophys. Res. Solid Earth 101,
672   3139–3156. https://doi.org/10.1029/95JB03446
673 Christensen, N.I., Mooney, W.D., 1995. Seismic velocity structure and composition of the continental
674   crust: A global view. J. Geophys. Res. Solid Earth 100, 9761–9788.
675   https://doi.org/10.1029/95JB00259
676 Clayton, R.W., Wiggins, R.A., 1976. Source shape estimation and deconvolution of teleseismic
677   bodywaves. Geophys. J. R. Astron. Soc. 47, 151–177. https://doi.org/10.1111/j.1365-
678   246X.1976.tb01267.x
679 Çubuk-Sabuncu, Y., Taymaz, T., Fichtner, A., 2017. 3-D crustal velocity structure of western Turkey:
680   Constraints from full-waveform tomography. Phys. Earth Planet. Inter. 270, 90–112.
681 Çubuk-Sabuncu, Y., Yolsal-Çevikbilen, S., Taymaz, T., 2014. Source Parameters of Bala-Sirapinar
682   (Central Turkey) Earthquakes of 2005-2008: Implications on Internal Deformations of the
683   Anatolian Plate. Tectonophysics 635, 125–153. https://doi.org/10.1016/j.tecto.2014.07.005
684 Darbyshire, F.A., 2003. Crustal structure across the Canadian High Arctic region from teleseismic
685   receiver function analysis. Geophys. J. Int. 152, 372–391. https://doi.org/10.1046/j.1365-
686   246X.2003.01840.x
687 Delph, J.R., Biryol, C.B., Beck, S.L., Zandt, G., Ward, K.M., 2015. Shear wave velocity structure of the
688   Anatolian Plate: anomalously slow crust in southwestern Turkey. Geophys. J. Int. 202, 261–
689   276. https://doi.org/10.1093/gji/ggv141
690 Dewey, J., Şengör, A.M.Cel., 1979. Aegean and surrounding regions: Complex multiplate and
691   continuum tectonics in a convergent zone. GSA Bull. 90, 84–92.
692   https://doi.org/10.1130/0016-7606(1979)90<84:AASRCM>2.0.CO;2
693 Eken, T., Bohnhoff, M., Bulut, F., Can, B., Aktar, M., 2013a. Crustal Anisotropy in the Eastern Sea of
694   Marmara Region in Northwestern TurkeyCrustal Anisotropy in the Eastern Sea of Marmara

695   Region in Northwestern Turkey. Bull. Seismol. Soc. Am. 103, 911–924.
696   https://doi.org/10.1785/0120120156
697 Eken, T., Tilmann, F., Mechie, J., Zhao, W., Kind, R., Su, H., Xue, G., Karplus, M., 2013b. Seismic
698   Anisotropy from SKS Splitting beneath Northeastern TibetShort Note. Bull. Seismol. Soc. Am.
699   103, 3362–3371. https://doi.org/10.1785/0120130054
700 Fichtner, A., Saygin, E., Taymaz, T., Cupillard, P., Capdeville, Y., Trampert, J., 2013a. The deep
701   structure of the North Anatolian Fault Zone. Earth Planet. Sci. Lett. 373, 109–117.
702   https://doi.org/10.1016/j.epsl.2013.04.027
703 Fichtner, A., Trampert, J., Cupillard, P., Saygin, E., Taymaz, T., Capdeville, Y., Villaseñor, A., 2013b.
704   Multiscale full waveform inversion. Geophys. J. Int. 194, 534–556.
705   https://doi.org/10.1093/gji/ggt118
706 Fouch, M.J., Rondenay, S., 2006. Seismic anisotropy beneath stable continental interiors. Phys. Earth
707   Planet. Inter. 158, 292–320.
708 Gaebler, P., Eken, T., Bektaş, H.Ö., Wegler, U., Taymaz, T., under review. Shear Wave Attenuation
709   along the central part of the North Anatolian Fault Zone. Bull. Seismol. Soc. Am.
710 Gans, C.R., Beck, S.L., Zandt, G., Biryol, C.B., Ozacar, A.A., 2009. Detecting the limit of slab break-off
711   in central Turkey: new high-resolution Pn tomography results. Geophys. J. Int. 179, 1566–
712   1572. https://doi.org/10.1111/j.1365-246X.2009.04389.x
713 Gudmundsson, A., 1999. Fluid overpressure and stress drop in fault zones. Geophys. Res. Lett. 26,
714   115–118.
715 Hannemann, K., Krüger, F., Dahm, T., Lange, D., 2016. Oceanic lithospheric S-wave velocities from
716   the analysis of P-wave polarization at the ocean floor. Geophys. J. Int. 207, 1796–1817.
717   https://doi.org/10.1093/gji/ggw342
718 Hurd, O., Bohnhoff, M., 2012. Stress-and Structure-Induced Shear-Wave Anisotropy along the 1999
719   Izmit Rupture, Northwest Turkey. Bull. Seismol. Soc. Am. 102, 2177–2188.
720 Jacobsen, B.H., Svenningsen, L., 2008. Enhanced uniqueness and linearity of receiver function
721   inversion. Bull. Seismol. Soc. Am. 98, 1756–1767. https://doi.org/10.1785/0120070180
722 Kahraman, M., Cornwell, D.G., Thompson, D.A., Rost, S., Houseman, G.A., Türkelli, N., Teoman, U.,
723   Altuncu Poyraz, S., Utkucu, M., Gülen, L., 2015. Crustal-scale shear zones and heterogeneous
724   structure beneath the North Anatolian Fault Zone, Turkey, revealed by a high-density
725   seismometer array. Earth Planet. Sci. Lett. 430, 129–139.
726   https://doi.org/10.1016/j.epsl.2015.08.014
727 Karabulut, H., Özalaybey, S., Taymaz, T., Aktar, M., Selvi, O., Kocaoğlu, A., 2003. A tomographic
728   image of the shallow crustal structure in the Eastern Marmara. Geophys. Res. Lett. 30, 2277.
729   https://doi.org/10.1029/2003GL018074
730 Karasözen, E., Özacar, A.A., Biryol, C.B., Beck, S.L., 2013. Seismicity, focal mechanisms and active
731   stress field around the central segment of the North Anatolian Fault in Turkey. Geophys. J.
732   Int. 196, 405–421.
733 Kaya, T., Kasaya, T., Tank, S.B., Ogawa, Y., Tunçer, M.K., Oshiman, N., Honkura, Y., Matsushima, M.,
734   2013. Electrical characterization of the North Anatolian Fault Zone underneath the Marmara
735   Sea, Turkey by ocean bottom magnetotellurics. Geophys. J. Int. 193, 664–677.
736 Kaymakçı, N., 2000. Tectono-stratigraphical evolution of the Çankırı basin (Central Anatolia, Turkey).
737   Utrecht University.
738 Kaymakçı, N., Özçelik, Y., White, S.H., Van Dijk, P.M., 2009. Tectono-stratigraphy of the Çankırı Basin:
739   late Cretaceous to early Miocene evolution of the Neotethyan suture zone in Turkey. Geol.
740   Soc. Lond. Spec. Publ. 311, 67–106.
741 Kaymakçı, N., White, S.H., Vandijk, P.M., 2003. Kinematic and structural development of the Çankiri
742   Basin (Central Anatolia, Turkey): a paleostress inversion study. Tectonophysics 364, 85–113.
743   https://doi.org/10.1016/S0040-1951(03)00043-X
744 Koulakov, I., Bindi, D., Parolai, S., Grosser, H., Milkereit, C., 2010. Distribution of Seismic Velocities
745   and Attenuation in the Crust beneath the North Anatolian Fault (Turkey) from Local

746   Earthquake Tomography. Bull. Seismol. Soc. Am. 100, 207–224.
747   https://doi.org/10.1785/0120090105

748 Langston, C.A., 1979. Structure under Mount Rainier, Washington, inferred from teleseismic body
749   waves. J. Geophys. Res. Solid Earth 84, 4749–4762.
750   https://doi.org/10.1029/JB084iB09p04749

751 Le Pichon, X., Şengör, A.M.C., Kende, J., İmren, C., Henry, P., Grall, C., Karabulut, H., 2015.
752   Propagation of a strike-slip plate boundary within an extensional environment: the
753   westward propagation of the North Anatolian Fault. Can. J. Earth Sci. 53, 1416–1439.
754   https://doi.org/10.1139/cjes-2015-0129

755 León Soto, G., Sandvol, E., Ni, J.F., Flesch, L., Hearn, T.M., Tilmann, F., Chen, J., Brown, L.D., 2012.
756   Significant and vertically coherent seismic anisotropy beneath eastern Tibet. J. Geophys. Res.
757   Solid Earth 117, B05308. https://doi.org/10.1029/2011JB008919

758 Liccardi, A., Eken, T., Agostnetti, N.P., Yolsal-Çevikbilen, S., Tilmann, F., Taymaz, T., 2018. Seismic
759   anisotropy in central North Anatolian Fault Zone and its implications on crustal deformation.
760   Phys. Earth Planet. Inter. 277, 99–112. https://doi.org/doi.org/10.1016/j.pepi.2018.01.012

761 Lophaven, S.N., Nielsen, H.B., Søndergaard, J., 2002. DACE-A Matlab Kriging toolbox, version 2.0.

762 Lyakhovsky, V., Ben-Zion, Y., Agnon, A., 2001. Earthquake cycle, fault zones, and seismicity patterns
763   in a rheologically layered lithosphere. J. Geophys. Res. Solid Earth 106, 4103–4120.

764 Menke, W., 1989. Geophysical Data Analysis: Discrete Inverse Theory. Academic Press.

765 Molnar, P., Dayem, K.E., 2010. Major intracontinental strike-slip faults and contrasts in lithospheric
766   strength. Geosphere 6, 444–467. https://doi.org/10.1130/GES00519.1

767 Najdahmadi, B., Bohnhoff, M., Ben-Zion, Y., 2016. Bimaterial interfaces at the Karadere segment of
768   the North Anatolian Fault, northwestern Turkey. J. Geophys. Res. Solid Earth 121, 931–950.

769 Nakamura, A., Hasegawa, A., Ito, A., Üçer, B., Bariş, Ş., Honkura, Y., Kono, T., Hori, S., Pektaş, R.,
770   Komut, T., Çelik, C., Işikara, A.M., 2002. P-wave Velocity Structure of the Crust and Its
771   Relationship to the Occurrence of the 1999 İzmit, Turkey, Earthquake and Aftershocks. Bull.
772   Seismol. Soc. Am. 92, 330–338. https://doi.org/10.1785/0120000803

773 Ottemöller, L., Midzi, V., 2003. The crustal structure of Norway from inversion of teleseismic receiver
774   functions. J. Seismol. 7, 35–48. https://doi.org/10.1023/A:1021294504092

775 Owens, T.J., Taylor, S.R., Zandt, G., 1987. Crustal structure at regional seismic test network stations
776   determined from inversion of broadband teleseismic P waveforms. Bull. Seismol. Soc. Am.
777   77, 631–662.

778 Papaleo, E., Cornwell, D., Rawlinson, N., 2018. Constraints on North Anatolian Fault Zone Width in
779   the Crust and Upper Mantle From S Wave Teleseismic Tomography. J. Geophys. Res. Solid
780   Earth 123, 2908–2922. https://doi.org/10.1002/2017JB015386

781 Papaleo, E., Cornwell, D.G., Rawlinson, N., 2017. Seismic tomography of the North Anatolian Fault:
782   New insights into structural heterogeneity along a continental strike-slip fault. Geophys. Res.
783   Lett. 44, 2017GL072726. https://doi.org/10.1002/2017GL072726

784 Paul, A., Karabulut, H., Mutlu, A.K., Salaün, G., 2014. A comprehensive and densely sampled map of
785   shear-wave azimuthal anisotropy in the Aegean–Anatolia region. Earth Planet. Sci. Lett. 389,
786   14–22.

787 Peng, Z., Ben-Zion, Y., 2004. Systematic analysis of crustal anisotropy along the Karadere—Düzce
788   branch of the North Anatolian fault. Geophys. J. Int. 159, 253–274.

789 Platt, J.P., Behr, W.M., 2011. Deep structure of lithospheric fault zones. Geophys. Res. Lett. 38,
790   L24308. https://doi.org/10.1029/2011GL049719

791 Polat, G., Özel, N.M., Koulakov, I., 2016. Investigating P- and S-wave velocity structure beneath the
792   Marmara region (Turkey) and the surrounding area from local earthquake tomography.
793   Earth Planets Space 68, 132. https://doi.org/10.1186/s40623-016-0503-4

794 Poyraz, S.A., Teoman, M.U., Türkelli, N., Kahraman, M., Cambaz, D., Mutlu, A., Rost, S., Houseman,
795   G.A., Thompson, D.A., Cornwell, D., 2015. New constraints on micro-seismicity and stress

796   state in the western part of the North Anatolian Fault Zone: Observations from a dense
797   seismic array. Tectonophysics 656, 190–201.
798   Reilinger, R., McClusky, S., Vernant, P., Lawrence, S., Ergintav, S., Cakmak, R., Ozener, H., Kadirov, F.,
799   Guliev, I., Stepanyan, R., Nadariya, M., Hahubia, G., Mahmoud, S., Sakr, K., ArRajehi, A.,
800   Paradissis, D., Al-Aydrus, A., Prilepin, M., Guseva, T., Evren, E., Dmitrotsa, A., Filikov, S.V.,
801   Gomez, F., Al-Ghazzi, R., Karam, G., 2006. GPS constraints on continental deformation in the
802   Africa-Arabia-Eurasia continental collision zone and implications for the dynamics of plate
803   interactions. J. Geophys. Res. Solid Earth 111, B05411.
804   https://doi.org/10.1029/2005JB004051
805   Rondenay, S., 2009. Upper Mantle Imaging with Array Recordings of Converted and Scattered
806   Teleseismic Waves. Surv. Geophys. 30, 377–405. https://doi.org/10.1007/s10712-009-9071-
807   5
808   Salaün, G., Pedersen, H.A., Paul, A., Farra, V., Karabulut, H., Hatzfeld, D., Papazachos, C., Childs, D.M.,
809   Pequegnat, C., Team, S., 2012. High-resolution surface wave tomography beneath the
810   Aegean-Anatolia region: constraints on upper-mantle structure. Geophys. J. Int. 190, 406–
811   420.
812   Sandvol, E., Seber, D., Barazangi, M., Vernon, F., Mellors, R., Al-Amri, A., 1998. Lithospheric seismic
813   velocity discontinuities beneath the Arabian Shield. Geophys. Res. Lett. 25, 2873–2876.
814   https://doi.org/10.1029/98GL02214
815   Schiffer, C., Jacobsen, B.H., Balling, N., Ebbing, J., Nielsen, S.B., 2015. The East Greenland
816   Caledonides—teleseismic signature, gravity and isostasy. Geophys. J. Int. 203, 1400–1418.
817   https://doi.org/10.1093/gji/ggv373
818   Schiffer, C., Stephenson, R., Oakey, G.N., Jacobsen, B.H., 2016. The crustal structure of Ellesmere
819   Island, Arctic Canada—teleseismic mapping across a remote intraplate orogenic belt.
820   Geophys. J. Int. 204, 1579–1600. https://doi.org/10.1093/gji/ggv539
821   Schildgen, T.F., Yıldırım, C., Cosentino, D., Strecker, M.R., 2014. Linking slab break-off, Hellenic
822   trench retreat, and uplift of the Central and Eastern Anatolian plateaus. Earth-Sci. Rev. 128,
823   147–168. https://doi.org/10.1016/j.earscirev.2013.11.006
824   Şengör, A.M.C., Tüysüz, O., İmren, C., Sakınç, M., Eyidoğan, H., Görür, N., Pichon, X.L., Rangin, C.,
825   2005. The North Anatolian Fault: A New Look. Annu. Rev. Earth Planet. Sci. 33, 37–112.
826   https://doi.org/10.1146/annurev.earth.32.101802.120415
827   Storti, F., Holdsworth, R.E., Salvini, F., 2003. Intraplate strike-slip deformation belts. Geol. Soc. Lond.
828   Spec. Publ. 210, 1–14.
829   Svenningsen, L., Jacobsen, B.H., 2007. Absolute S-velocity estimation from receiver functions.
830   Geophys. J. Int. 170, 1089–1094. https://doi.org/10.1111/j.1365-246X.2006.03505.x
831   Tarantola, A., Valette, B., 1982. Generalized nonlinear inverse problems solved using the least
832   squares criterion. Rev. Geophys. 20, 219–232. https://doi.org/10.1029/RG020i002p00219
833   Taylor, G., Rost, S., Houseman, G., 2016. Crustal imaging across the North Anatolian Fault Zone from
834   the autocorrelation of ambient seismic noise. Geophys. Res. Lett. 43, 2016GL067715.
835   https://doi.org/10.1002/2016GL067715
836   Taymaz, T., Jackson, J., McKenzie, D., 1991. Active tectonics of the north and central Aegean Sea.
837   Geophys. J. Int. 106, 433–490. https://doi.org/10.1111/j.1365-246X.1991.tb03906.x
838   Taymaz, T., Kasahara, J., Hirn, A., Sato, T., 2001. Investigations of micro-earthquake activity within
839   the Sea of Marmara and surrounding regions by using ocean bottom seismometers (OBS)
840   and land seismographs: initial results, in: Scientific Activities 2001 Symposia -Extended
841   Abstracts Book. Presented at the Scientific Activities 2001 Symposia, May 8, 2001, ATLAS
842   DBR-Offset Printing House, Istanbul Technical University, Faculty of Mines, pp. 42–51.
843   Taymaz, T., Wright, T.J., Yolsal, S., Tan, O., Fielding, E., Seyitoğlu, G., 2007a. Source characteristics of
844   the 6 June 2000 Orta–Çankırı (central Turkey) earthquake: a synthesis of seismological,
845   geological and geodetic (InSAR) observations, and internal deformation of the Anatolian
846   plate. Geol. Soc. Lond. Spec. Publ. 291, 259–290. https://doi.org/10.1144/SP291.12

847   Taymaz, T., Yilmaz, Y., Dilek, Y., 2007b. The geodynamics of the Aegean and Anatolia: introduction.
848   Geol. Soc. Lond. Spec. Publ. 291, 1–16. https://doi.org/10.1144/SP291.1

849   Vanacore, E.A., Taymaz, T., Saygin, E., 2013. Moho structure of the Anatolian Plate from receiver
850   function analysis. Geophys. J. Int. 193, 329–337. https://doi.org/10.1093/gji/ggs107

851   Warren, L.M., Beck, S.L., Biryol, C.B., Zandt, G., Özacar, A.A., Yang, Y., 2013. Crustal velocity structure
852   of Central and Eastern Turkey from ambient noise tomography. Geophys. J. Int. 194, 1941–
853   1954. https://doi.org/10.1093/gji/ggt210

854   Weber, M., Abu-Ayyash, K., Abueladas, A., Agnon, A., Al-Amoush, H., Babeyko, A., Bartov, Y.,
855   Baumann, M., Ben-Avraham, Z., Bock, G., Bribach, J., El-Kelani, R., Förster, A., Förster, H.-J.,
856   Frieslander, U., Garfunkel, Z., Grunewald, S., Götze, H.J., Haak, V., Haberland, C., Hassouneh,
857   M., Helwig, S., Hofstetter, A., Jäckel, K.-H., Kesten, D., Kind, R., Maercklin, N., Mechie, J.,
858   Mohsen, A., Neubauer, F.M., Oberhänsli, R., Qabbani, I., Ritter, O., Rümpker, G., Rybakov,
859   M., Ryberg, T., Scherbaum, F., Schmidt, J., Schulze, A., Sobolev, S., Stiller, M., Thoss, H.,
860   Weckmann, U., Wylegalla, K., 2004. The crustal structure of the Dead Sea Transform.
861   Geophys. J. Int. 156, 655–681. https://doi.org/10.1111/j.1365-246X.2004.02143.x

862   Wiechert, E., Zoeppritz, K., 1907. Ueber erdbebenwellen. Nachrichten Von Ges. Wiss. Zu Gött.
863   Math.-Phys. Kl. 1907, 415.

864   Wilson, M., Neumann, E.-R., Davies, G.R., Timmerman, M.J., Heeremans, M., Larsen, B.T., 2004.
865   Permo-Carboniferous magmatism and rifting in Europe: introduction. Geol. Soc. Lond. Spec.
866   Publ. 223, 1–10.

867   Yolsal-Çevikbilen, S., Biryol, C.B., Beck, S., Zandt, G., Taymaz, T., Adıyaman, H.E., Özacar, A.A., 2012.
868   3-D crustal structure along the North Anatolian Fault Zone in north-central Anatolia revealed
869   by local earthquake tomography. Geophys. J. Int. 188, 819–849.
870   https://doi.org/10.1111/j.1365-246X.2011.05313.x

871   Zhao, D., 2015. Multiscale seismic tomography. Springer.

872   Zhu, L., 2000. Crustal structure across the San Andreas Fault, southern California from teleseismic
873   converted waves. Earth Planet. Sci. Lett. 179, 183–190. https://doi.org/10.1016/S0012-
874   821X(00)00101-1

875

876

877   Table 1: Station information

Station	Latitude	Longitude	Array	No. events	Station	Latitude	Longitude	Array	No. events
ALIC	40.978	33.487	NAF	47	KIZI	40.048	36.536	NAF	37
ALIN	41.061	32.879	NAF	54	KUYL	41.59	34.332	NAF	73
ALOR	41.301	32.87	NAF	40	KUZA	40.441	36.248	NAF	85
ARSL	40.955	35.887	NAF	28	KUZO	40.904	32.861	NAF	81
BAGB	40.278	36.41	NAF	65	OGUR	41.109	35.165	NAF	65
BEDI	41.121	33.506	NAF	56	PANC	40.647	34.301	NAF	67
BEKI	41.315	34.263	NAF	62	PELI	41.113	34.299	NAF	73
BOKE	40.552	36.211	NAF	19	SEYH	40.856	32.9	NAF	70
CAKM	40.015	37.367	NAF	60	SYUN	40.838	33.529	NAF	98
CALT	41.328	35.125	NAF	57	YESI	40.405	37.229	NAF	21
CAYA	40.373	34.269	NAF	20	YIKI	40.748	35.954	NAF	52
CRLU	40.064	34.357	NAF	40	ANT	39.87	32.79	GSN	51
CUKU	40.604	33.441	NAF	31	CANT	40.61	33.62	KO	27
DERE	41.477	35.064	NAF	33	CDK	40.97	32.18	RS	51
DUMA	40.918	35.14	NAF	51	CORM	40.18	34.63	KO	78
EKIN	41.147	35.787	NAF	22	ILGA	41.05	33.72	NEMC	34
GOCE	39.743	34.348	NAF	113	KOZK	39.66	34.87	KO	29
HASA	41.469	33.565	NAF	72	KURC	41.85	32.74	KO	29
INCE	40.581	32.906	NAF	61	KVT	41.08	36.05	KO	24
INSU	39.842	35.366	NAF	39	POL	39.62	32.06	RS	31
ISKE	40.764	37.067	NAF	18	RSDY	40.4	37.33	KO	8
KARA	40.688	35.245	NAF	49	SNOP	42.02	35.21	KO	29
KARG	40.291	33.552	NAF	8	SVSK	39.92	36.99	KO	22
KAVA	40.28	32.878	NAF	12	TOKT	40.32	36.54	KO	67
KGAC	40.941	34.323	NAF	52	YOZ	39.64	35.32	KO	37
KIYI	40.131	35.316	NAF	48					
NAF=North Anatolian Fault Zone array; GSN=Global Seismic Network; KO=Kandilli Observatory & Earthquake Research Institute; RS=RESIF-SISMOB; NEMC=National Earthquake Monitoring Center (NEMC) in Turkey									

878

879

880
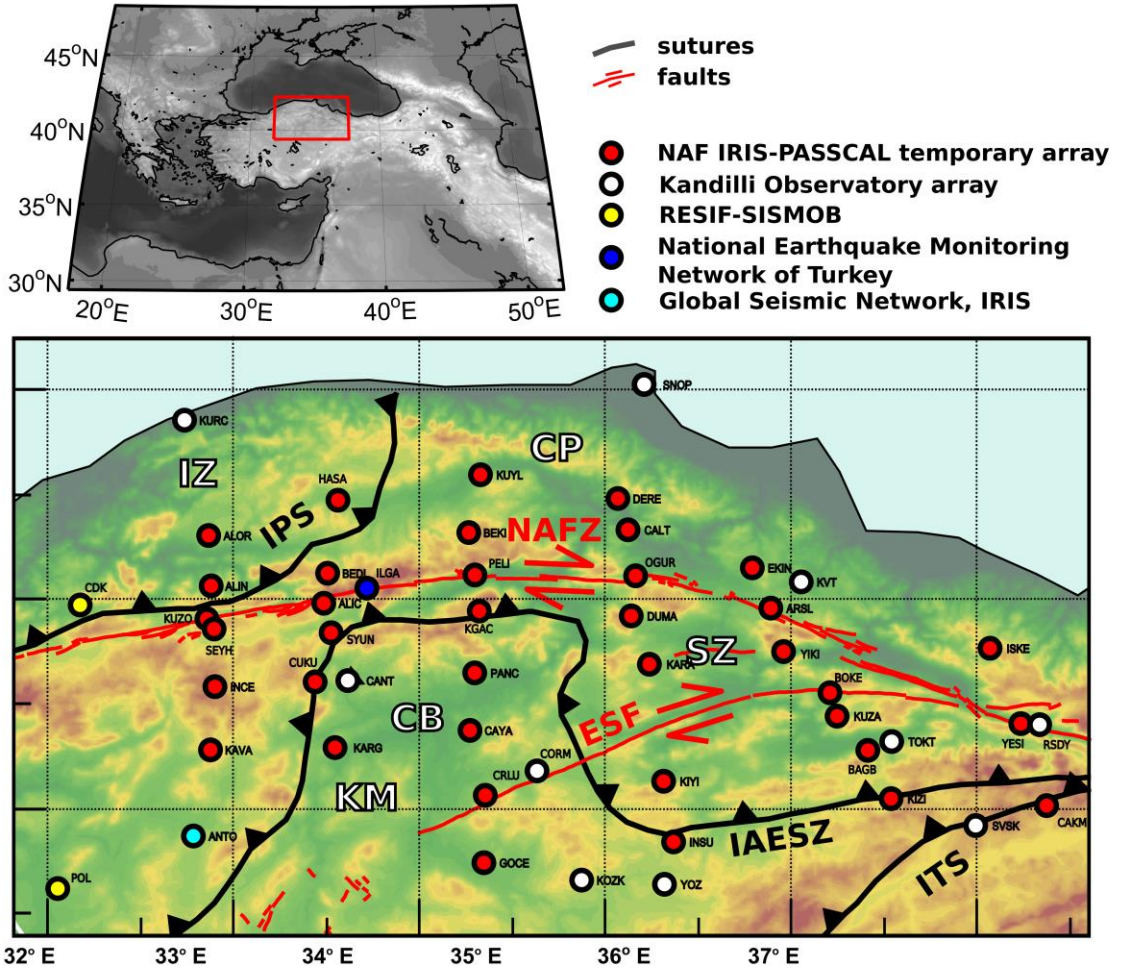
Figure 1: Outline of the study area within the broader eastern Mediterranean region (above)
and closeup (lower panel), with topography from ETOPO1 (Amante and Eakins, 2009)*.*
Major faults are indicated in red. Suture zones, modified after Kaymakçı et al. (2003), are
shown in grey. CB, Çankırı Basin; CP, Central Pontides; ESF, Ezinepazari-Sungurlu Fault;
IAESZ, Izmir- Ankara-Erzincan Suture Zone; IPS, Intra-Pontide Suture; IZ, Istanbul
Zone; ITS, Intra-Tauride Suture; KM, Kırşehir Massif; NAF, North Anatolian Fault;.SZ
Sakarya Zone.

881
882
883
884
885
886
887

888

889

890

891

892

893

894
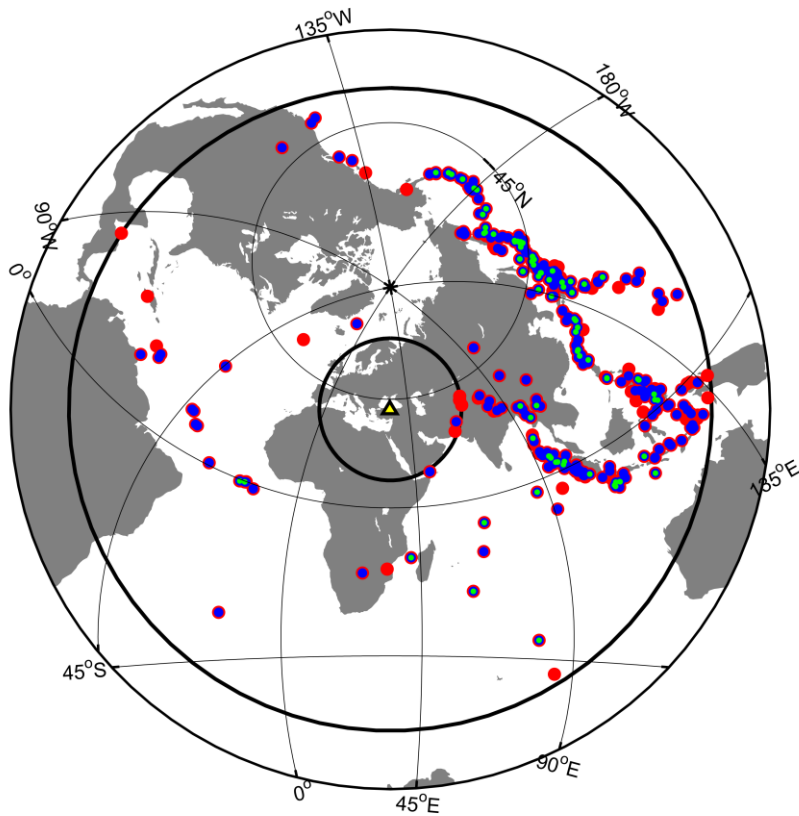
Figure 2: Distribution of all the teleseismic events used in this study. The map is centred on the geographical centroid of the seismic network (yellow triangle). The thick black circle marks epicentral distances of 30° (inner circle) and 100° (outer circle). Red dots are events of magnitude ≥7, blue dots are earthquakes of magnitude between 6 and 7, and green dots are all earthquakes with a magnitude <6. A detailed list of all the earthquakes used in our analysis is provided in Supplementary File S2.

901

902

903
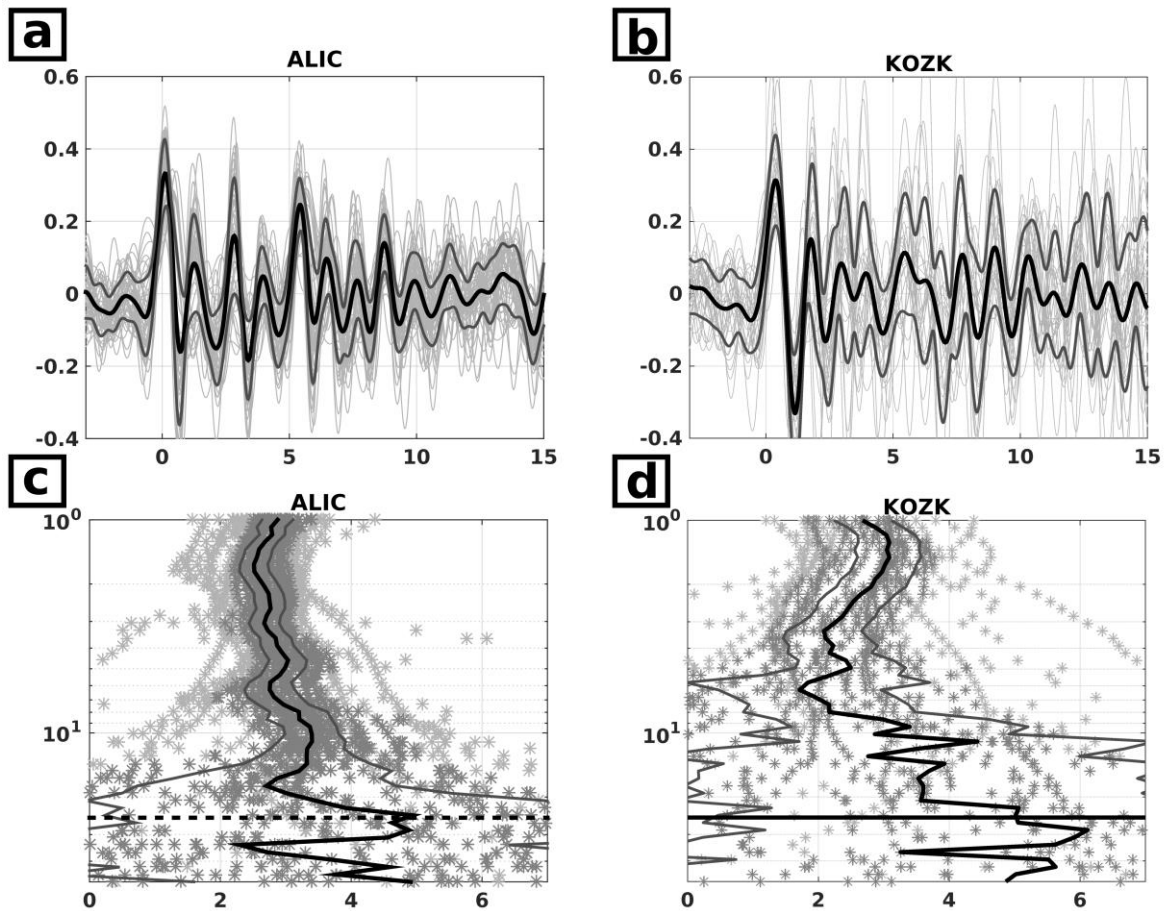
904

905 *Figure 3: Examples of receiver function (a,b) and Vs_{app} (c,d) for a seismic station of high*

906 *quality (ALIC, a,c) and lower quality (KOZK, b,d). The receiver function stack is shown as*

907 *a thick black line, with the standard deviation in dark grey. All individual receiver functions*

908 *are plotted in light grey in the background. The median Vs_{app} curves are shown in black,*

909 *with the standard deviation in dark grey. Individual Vs_{app} values are shown as grey stars,*

910 *with those within 68% confidence interval around the median shown in darker grey. The*

911 *horizontal stippled black line indicates the limit of 25 sec used for the inversion.*

912

913
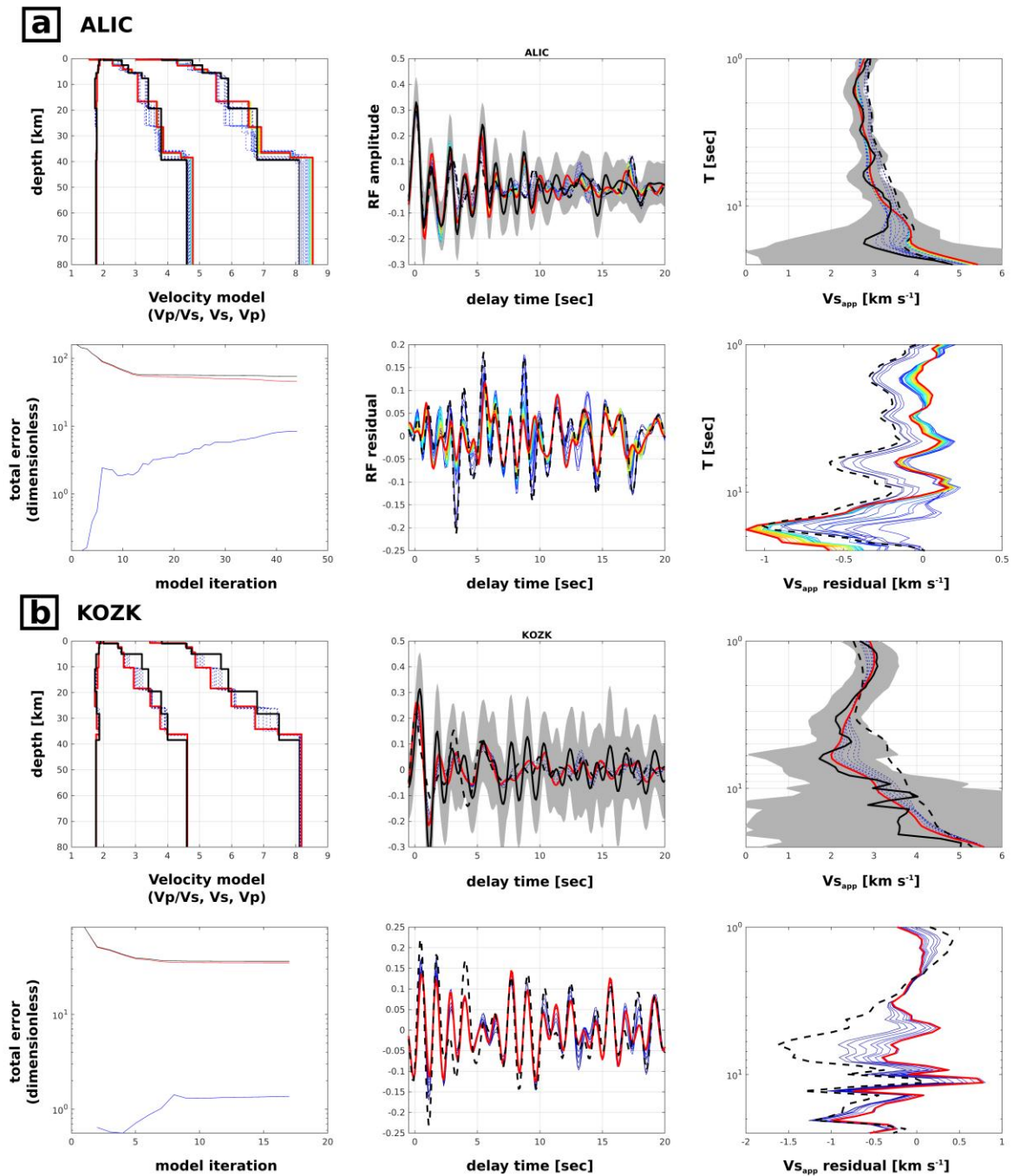
Figure 4: Examples of receiver function-Vs$_{app}$ inversion results for a high-quality station (ALIC, a) and a lower-quality station (KOZK, b). Different colours indicate the progression of the inversion in each panel. Blue colours denote early iterations, whereas reds denote later iterations. Since the inversion is stopped as soon as the inversion converges towards a constant model, not all models reach the maximum number of iterations of 50. The last iteration is shown by the thick red line in all plots. Upper left: The starting velocity model is denoted by a solid black line. Upper middle: Iterations over the receiver functions fit, with the solid black line representing the observed receiver function, the dashed black line

922   *denoting the RF for the starting model and the red thick line denoting the RF for the model*

923   *of the last iteration. The grey shading marks the standard deviation at each receiver function*

924   *time step. Upper right: Iterations over the Vs_{app} curve fits, with the solid black line*

925   *representing the observed Vs_{app}, the dashed black line denoting the Vs_{app} for the starting*

926   *model and the red line denoting the Vs_{app} for the model of the last iteration. The grey shading*

927   *marks the standard deviation at each period of the Vs_{app}-curve. Lower left: development of*

928   *the inversion error at each iteration, with the total error in black, the data error (receiver*

929   *functions and Vs_{app}) in red and the model error in blue. Lower middle: Residual receiver*

930   *function for each iteration. Stippled black line denotes the starting model and the solid red*

931   *line the model of the last iteration. Lower right: Residual Vs_{app} curve for each iteration.*

932   *Stippled black line denotes the starting model and the solid red line the model of the last*

933   *iteration.*

934

935

936

937

938
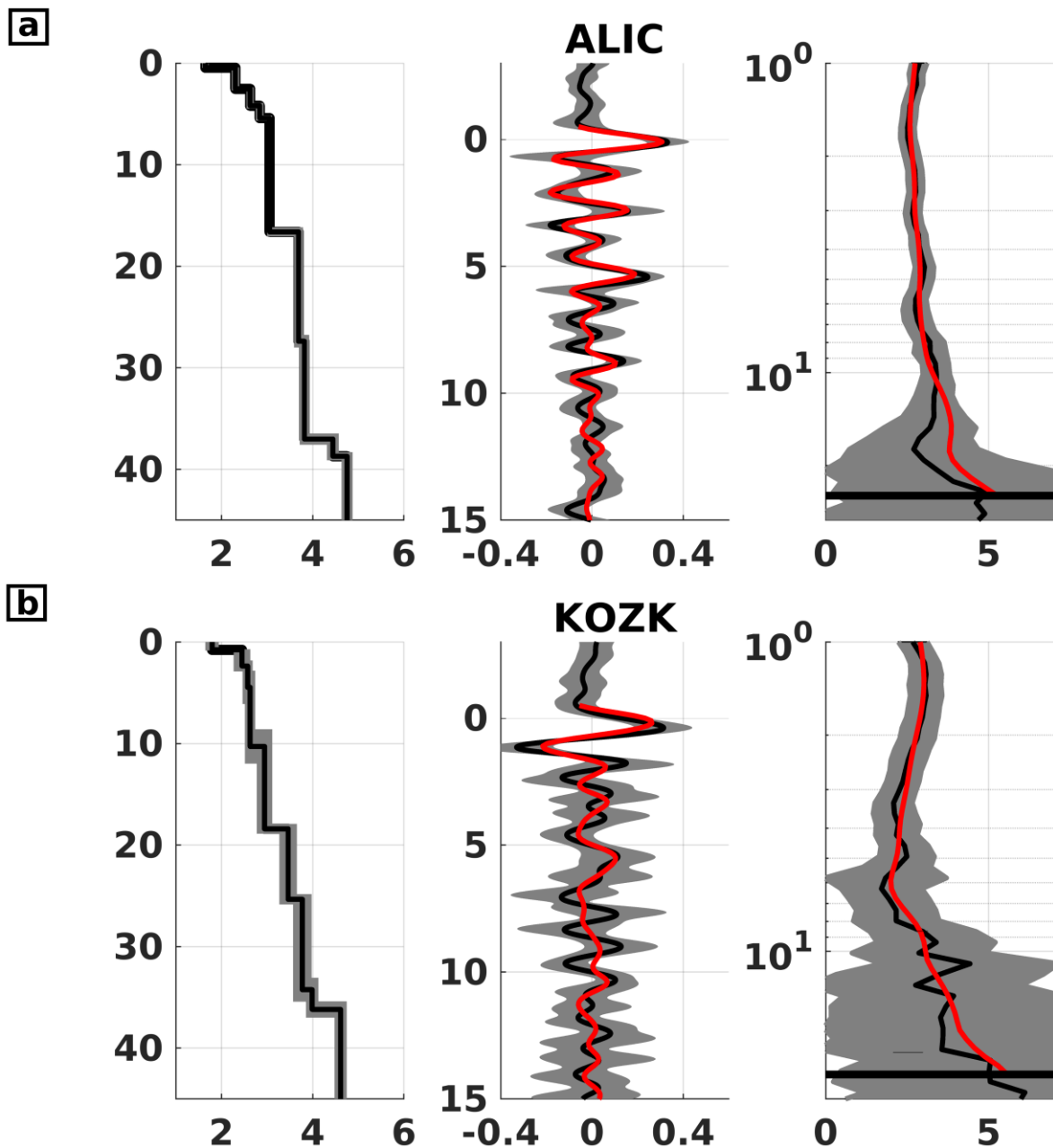
Figure 5. Examples for the final velocity model (left panel), with the corresponding receiver function fit (middle panel) and the Vs_{app} fit (right panel), for stations ALIC (a) and KOZK (b). Black lines in the middle and right panel show the observed data, red lines represent the best fits, and grey shading are the model error (left) and the observed standard deviations of the receiver functions (middle) and Vs_{app} (right).

944

945

946

947

948
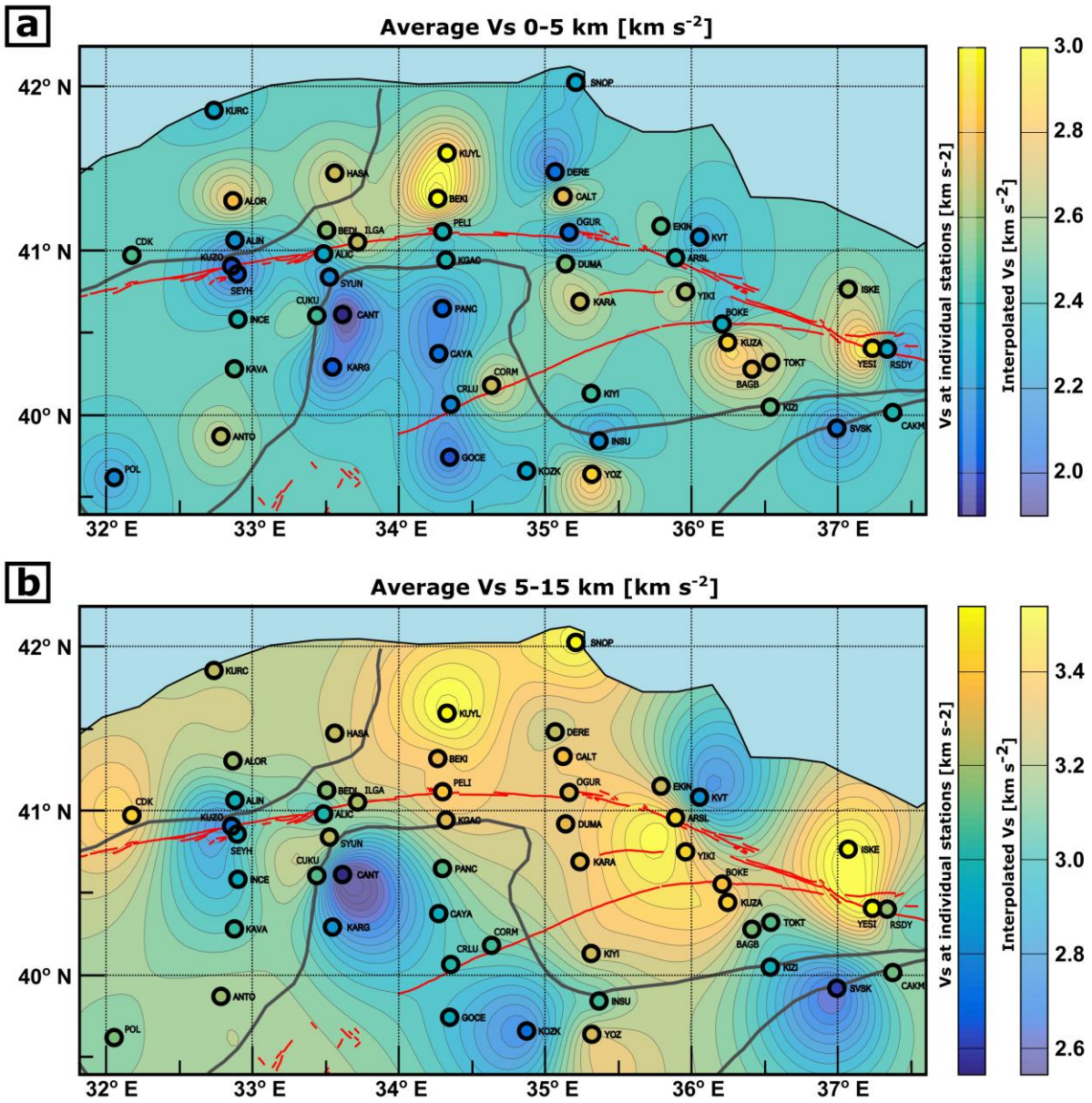
Figure 6: Inversion results in terms of S-wave velocities (a) in the upper 5 km of the crust, and (b) in the 5-15 km depth range. The results are shown at individual stations (coloured dots, see left colour bar), and as an interpolated basemap built by kriging the 1-D velocity models obtained at each station (background colours, see right colour bar).

949

950

951

952

953

954

955

Average Vp-Vs ratio (0-15 km) and seismicity (0-20 km)

956
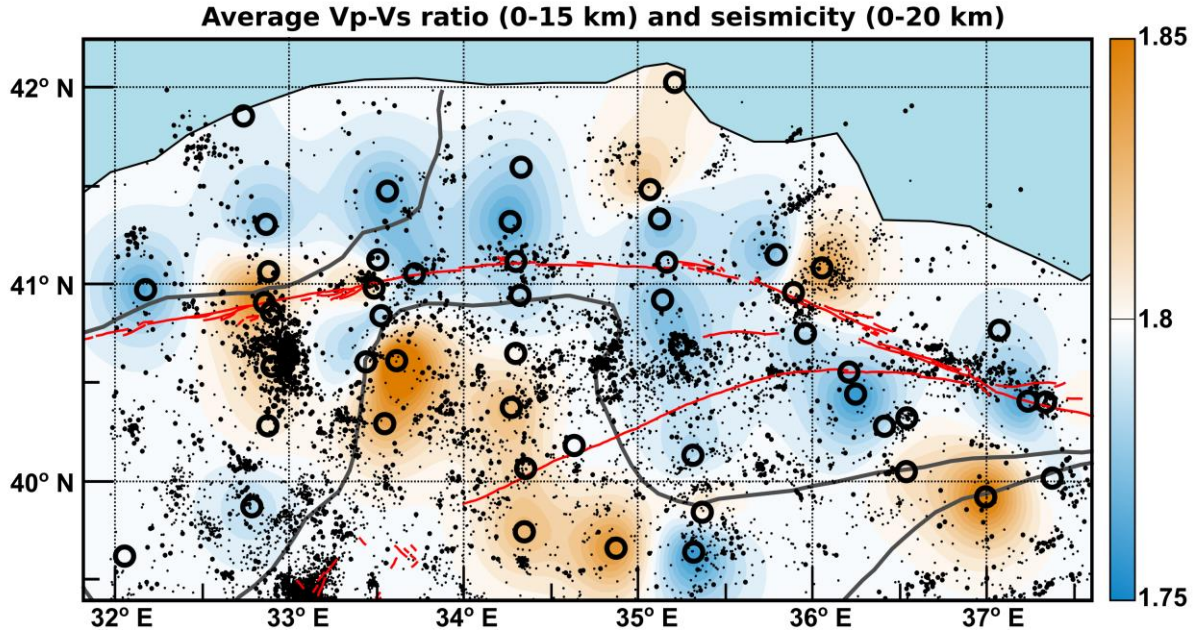
Figure 7: Map of seismicity and Vp/Vs ratio. Seismicity includes earthquakes with
magnitudes greater than 1 (black dots of three sizes: small M<3, medium M=3-4, large
M>=4) that occurred between 2005-2018 in the upper 20 km of the study area. The basemap
is built by kriging Vp/Vs ratios in the 0-15 km depth range obtained at individual stations.
Major faults are denoted by red lines. Sutures are shown as grey lines. Locations, depths and
magnitudes of the plotted earthquakes were provided by the Kandilli Observatory and
Earthquake Research Institute (see www.koeri.boun.edu.tr). Black circles indicate station
locations.

a Sedimentary thickness [km]

b Depth to crystalline basement [km]

c Moho depth [km]

965
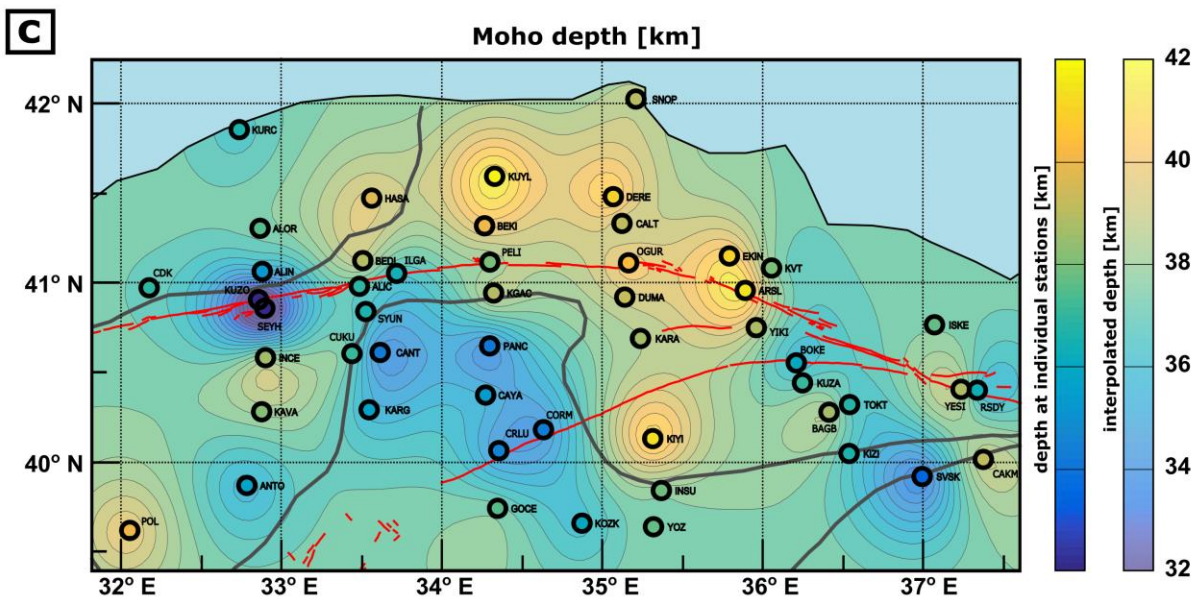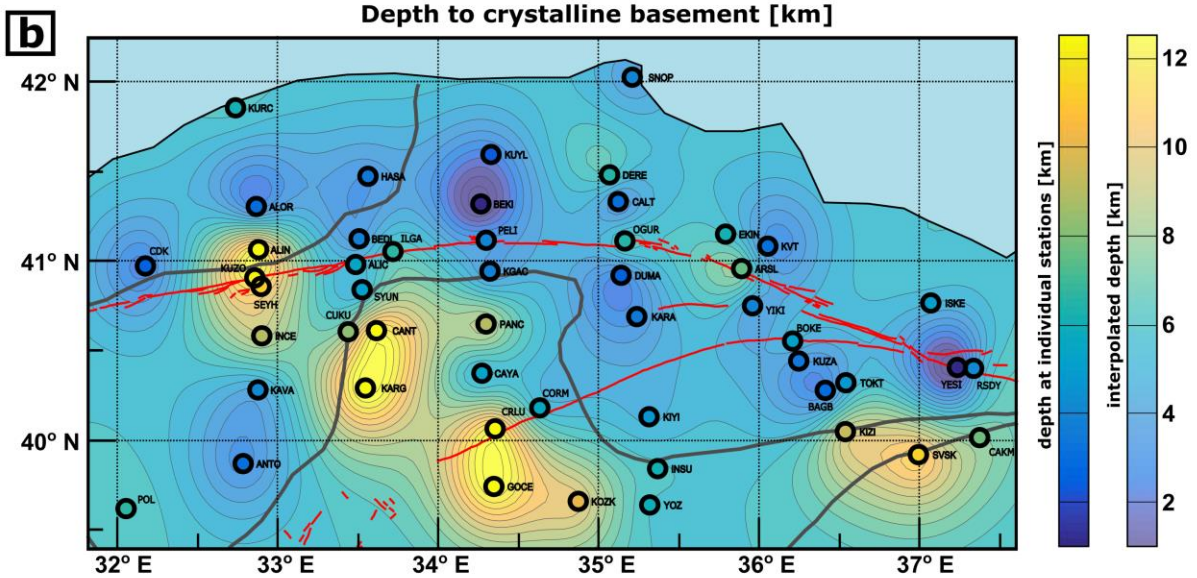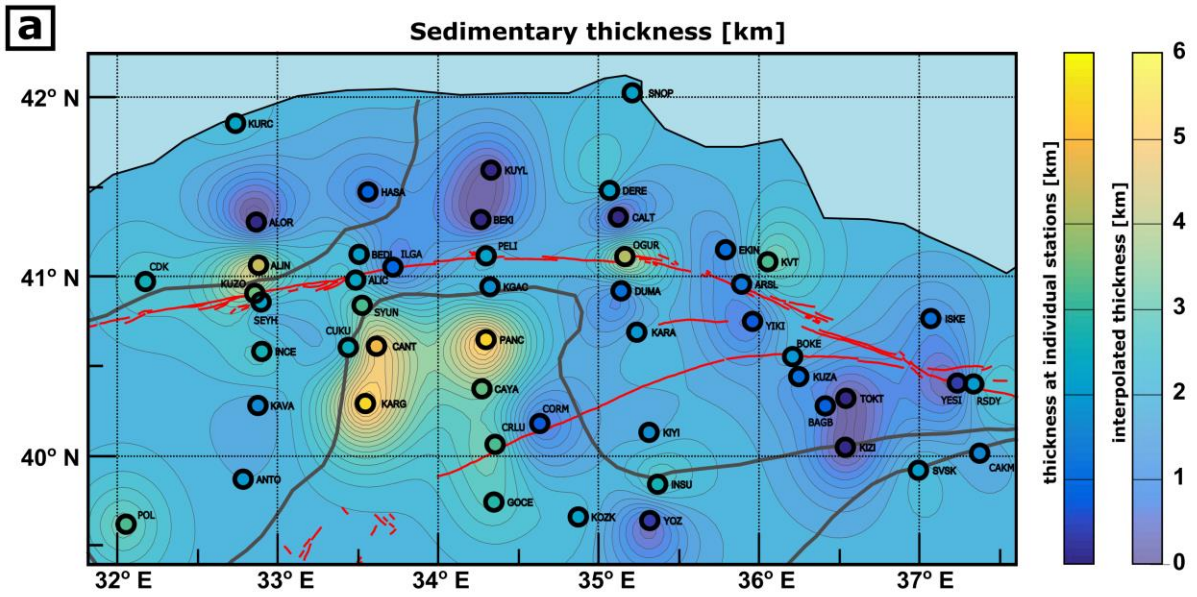
966   *Figure 8: Maps of inferred seismic structures across the study area, in relation to major*
967   *faults (red lines) and sutures (grey line). (a) Thickness of the uppermost low-velocity*
968   *sedimentary layer. (b) Depth to crystalline basement (or thickness of sediments and*
969   *metasediments). (c) Moho depth. The thicknesses/depths are shown at individual stations*
970   *(coloured dots, see left colour bar), and as an interpolated base map built by kriging the*
971   *values obtained at each station (background colours, see right colour bar).*

972

973

974

975

976

977

978
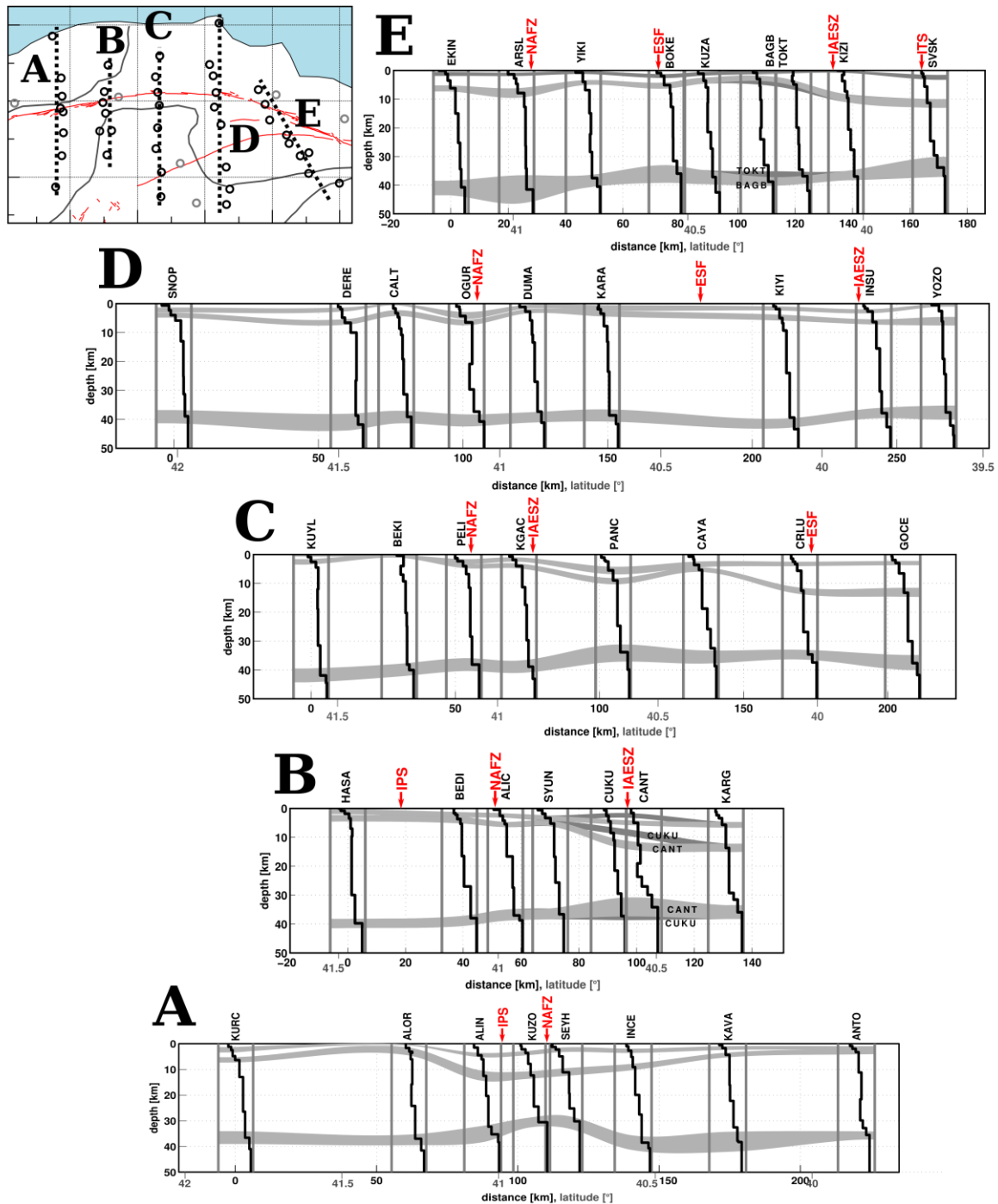
Figure 9. Five N-S profiles through the study area showing the 1D S-wave velocity profiles from joint inversion. Inset shows the outline of the study area, as well as the locations of the five profiles (A-E) and the seismic stations (black circles are stations used and grey circles are stations not used in the profiles). The approximate location of the North Anatolian Fault Zone (NAFZ), the Intra Pontide Suture (IPS), the Izmir- Ankara-Erzincan Suture Zone (IAESZ) and the Ezinepazari-Sungurlu Fault (ESF) are marked in the profiles. The grey bands in the background represent the three main interpreted interfaces, including the

986   *model error. These interfaces are, from top to bottom: base of the uppermost low-velocity*

987   *sedimentary layer, base of the crystalline basement, and the Moho. Note that, in two*

988   *instances, pairs of very closely spaced stations were used for the interpretation. In this case,*

989   *we spatially separated the station from another and also separated the interpretation from*

990   *each station for visualisation purposes: CUKU and TOKT are in dark grey, whereas CANT*

991   *and BAGB are in light grey. The velocity profiles are plotted in individual grey boxes for*

992   *each station along the profile, with vertical grey lines marking S-wave velocities of 1 km/s*

993   *and 4.8 km/s.*

994

995
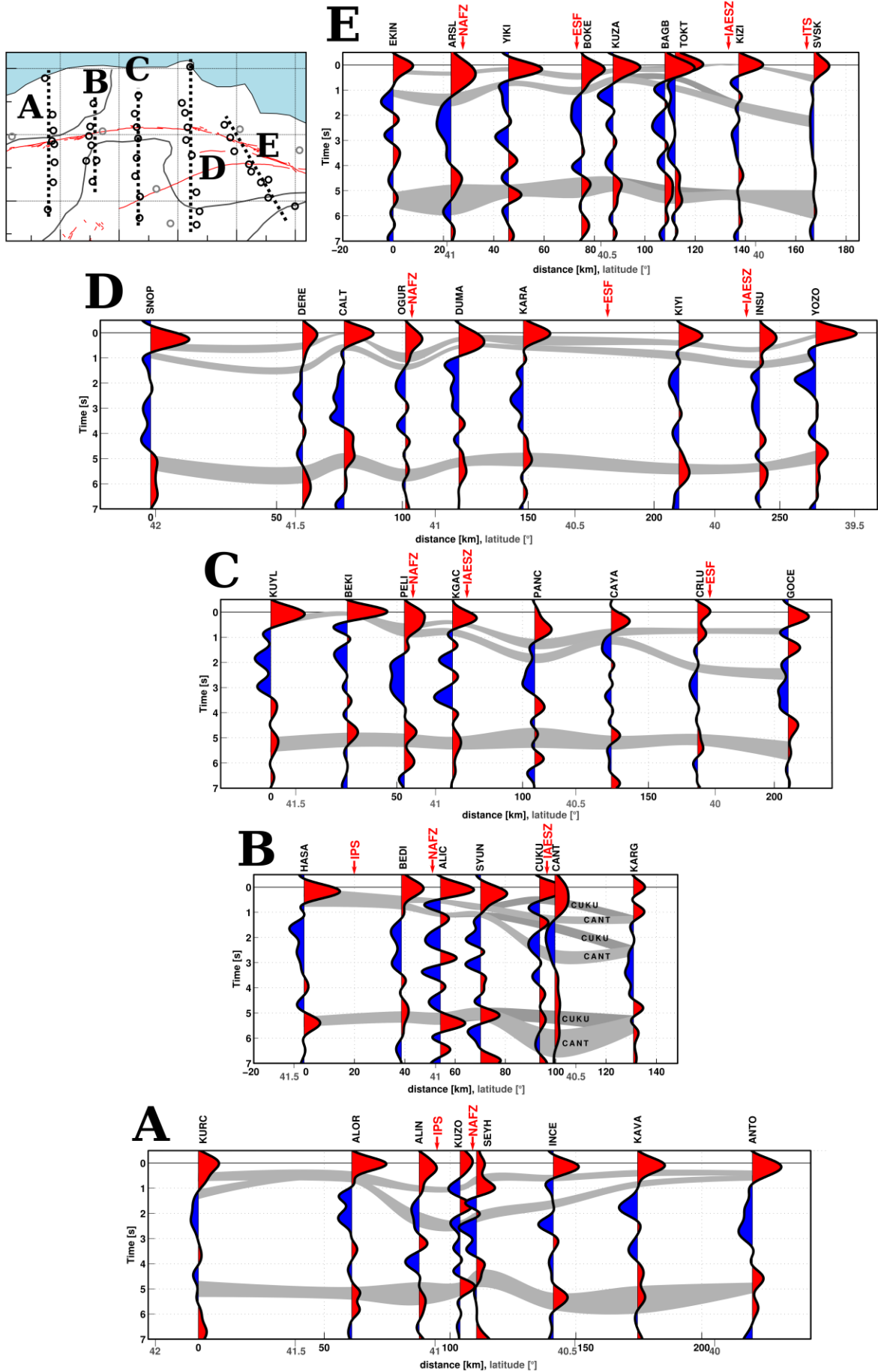
Figure 10. Same N-S profiles as for figure 9 showing the receiver function waveforms, along with the interpreted interfaces and their error bars in the delay-time domain. For details see caption of figure 9. At most stations, the interfaces correspond to clear signals in the receiver function waveform. However, there are a few cases where a clear signal is missing, which can be explained by a combination of generally weaker Moho discontinuities (gradients or the presence of high velocity lower crust) and the interference with sedimentary or intra-crustal multiples. Consistent with this explanation, weak Moho signals tend to be associated with a large sedimentary thickness (e.g. stations CUKU, CANT, PANC, OGUR, KIZI, SVSK). It should be noted that the receiver function delay time shown in this figure are depended on but neither equivalent nor proportional to depth. For example, the large Moho delay time at station CANT, in profile B, is due to a very thick sedimentary basin rather that large Moho depth.
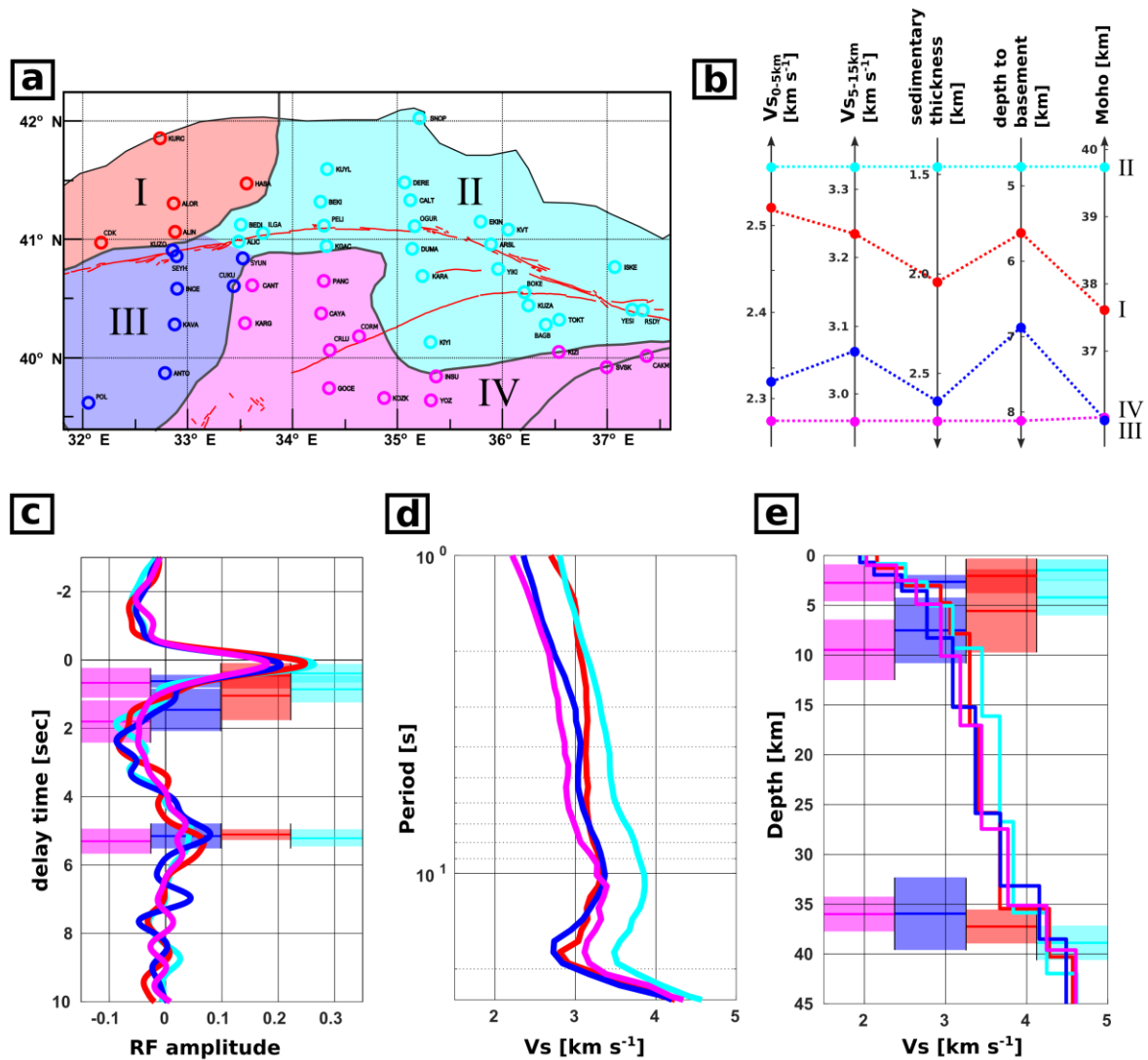
Figure 11: Summary of inversion results for the study area. (a) The study area is divided into four domains (I – red, II – light blue, III – dark blue, and IV – magenta). (b) Mean values of seismic properties and structures for each domain: S-wave velocity in the upper 5 km, the S-wave velocity in the 5-15 km depth range, inferred sedimentary thickness, inferred depth to basement and inferred Moho depth. It is apparent that domain IV exhibits the lowest velocities, shallowest Moho and deepest basins. It is followed by domain III, whereas the northern portion of the study area (domains I-II) exhibit generally high uppermost velocities, shallow basins and deep Moho. (c) Receiver function stacks for each domain. Note the clearly lower P-wave amplitudes for domains III-IV, compared to domains I-II, indicating low uppermost velocities in the south of the study area. Horizontal bars mark the average estimate of the sedimentary thickness, depth to basement and depth to Moho (converted to delay time) and shaded areas mark the respective variation in each region. (d) Mean Vs_{app} curves for each domain. Domains III-IV show lower uppermost S-wave
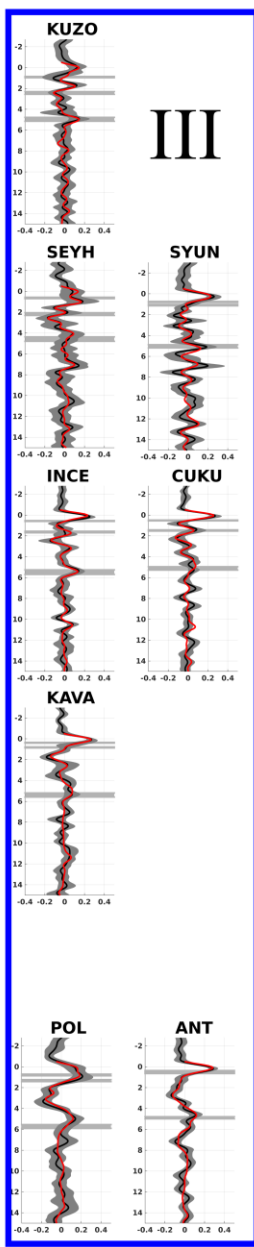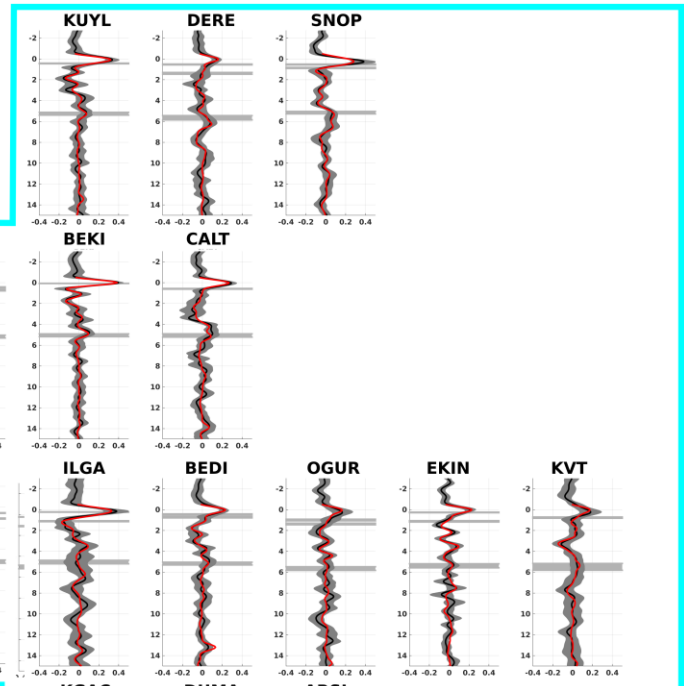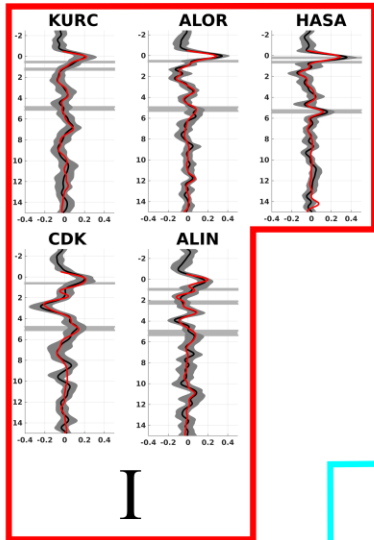
1023   *velocities compared to domains I-II. (e) S-wave velocity-depth profiles for each region, in*

1024   *which every of the eight model layers is averaged. Horizontal bars mark the average estimate*

1025   *of the sedimentary thickness, depth to basement and depth to Moho and shaded areas mark*

1026   *the respective variation in each region.*

1027

1028

1029

1030
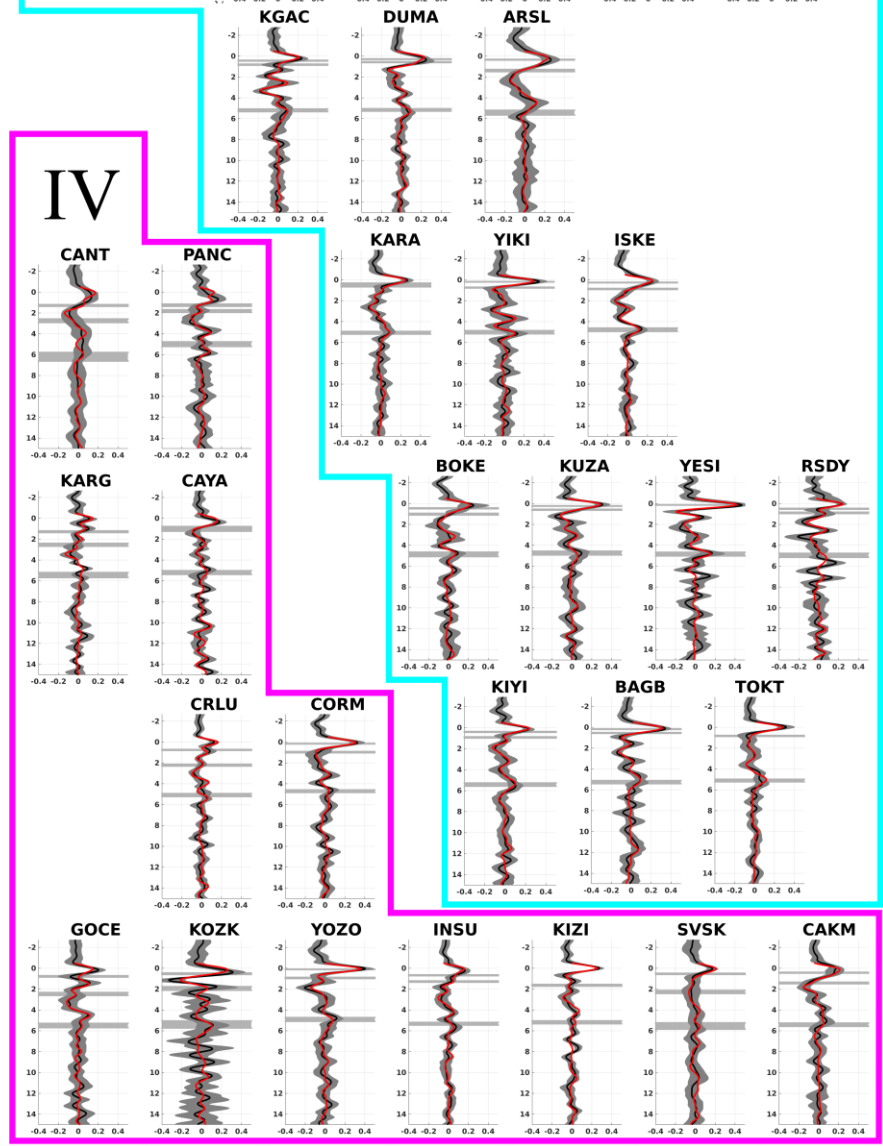
1032   *Figure 12: Receiver function stacks of all stations arranged in their approximate station*

1033   *geometry and sorted in their respective region (red – region I, cyan – region II, blue – region*

1034   *III, magenta – region IV). Black lines show the observed data, red lines represent the best*

1035   *fits, and grey shading are the observed standard deviations of the receiver functions. Grey*

1036   *shaded horizontal bars represent the estimates of sedimentary thickness, depth to basement*

1037   *and Moho depth converted to delay time – the thickness of the bar represents the*

1038   *mathematical error on these interfaces from the inversion. Each individual axis is identical*
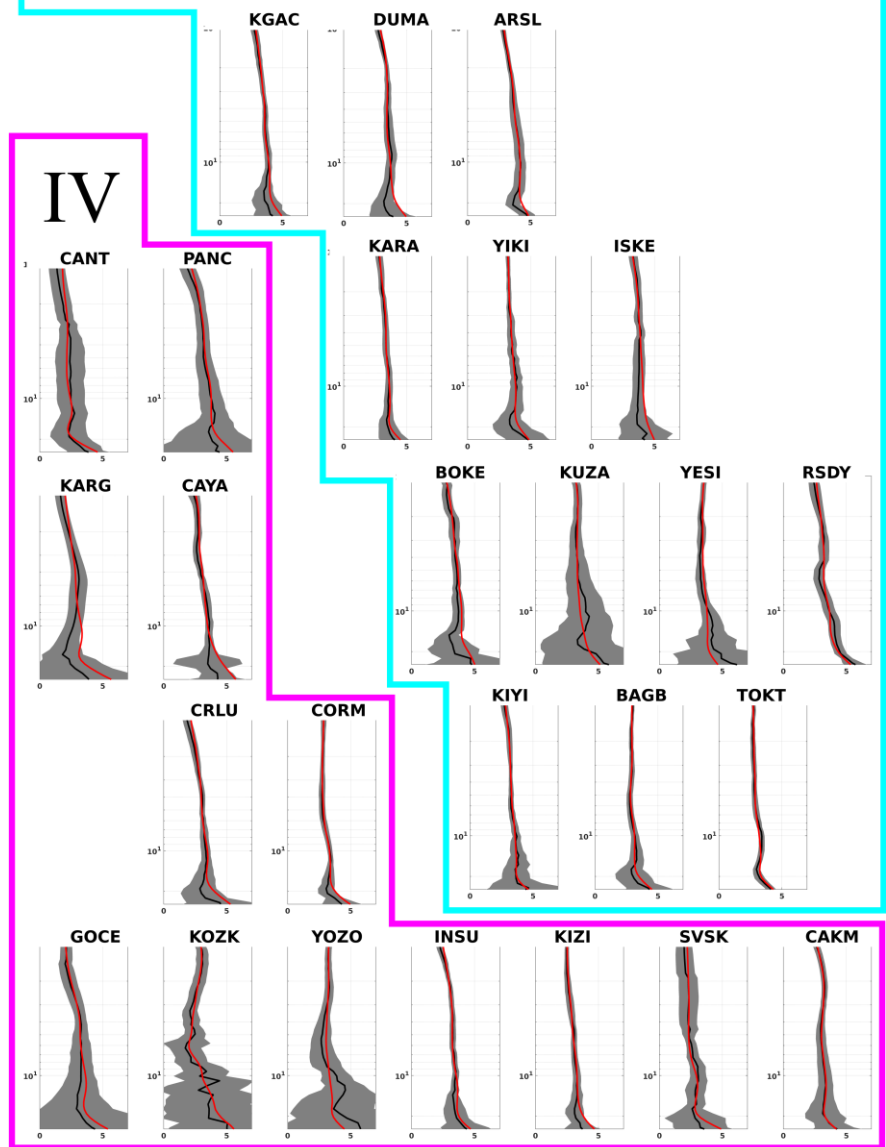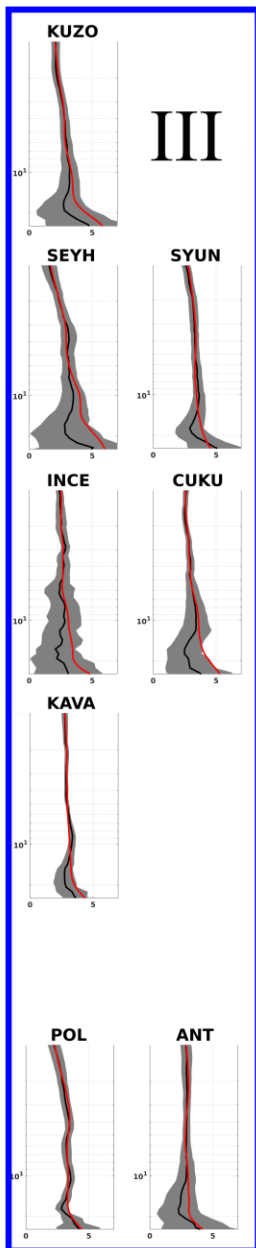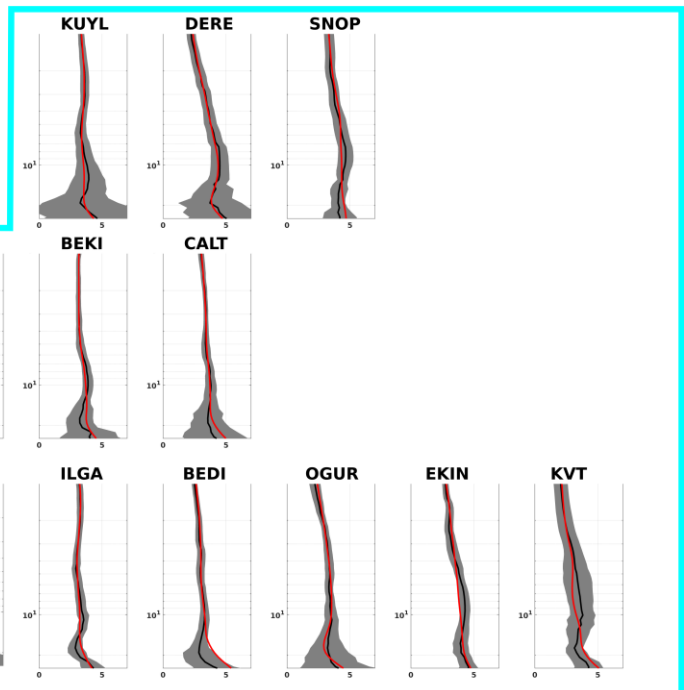
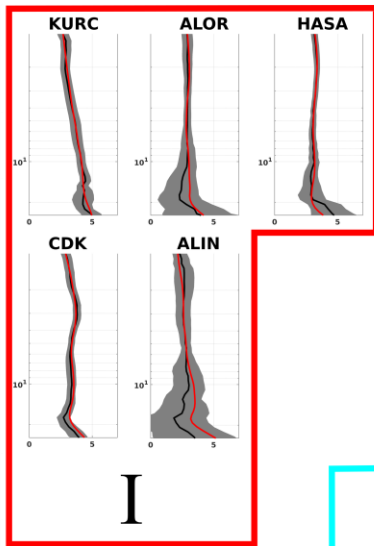1039   *to the axes in Figure 5, middle panels.*

1040

1041

1042

1043

1044

1046　　*Figure 13. Vs$_{app}$ curves of all stations arranged in their approximate station geometry and*

1047　　*sorted in their respective region (red – region I, cyan – region II, blue – region III, magenta*

1048　　*– region IV). Black lines show the observed data, red lines represent the best fits, and grey*

1049　　*shading are the observed standard deviations of the Vs$_{app}$. Each individual axis is identical*

1050　　*to the axes in Figure 5, right panel.*

1051

1052

1053